AIChE WILEY InterScience DISCOVER SOMETHING GREAT

# Drops, Slugs, and Flooding in Polymer Electrolyte Membrane Fuel Cells

**Erin Kimball, Tamara Whitaker, Yannis G. Kevrekidis, and Jay B. Benziger**
Dept. of Chemical Engineering, Princeton University, Princeton, NJ 08544

*DOI 10.1002/aic.11464*
*Published online March 26, 2008 in Wiley InterScience (www.interscience.wiley.com).*

*The process of flooding has been examined with a single-channel fuel cell that permits direct observation of liquid water motion and local current density. As product water flows through the largest pores in the hydrophobic GDL, drops detach from the surface, aggregate, and form slugs. Flooding in polymer electrolyte membrane (PEM) fuel cells occurs when liquid water slugs accumulate in the gas flow channel, inhibiting reactant transport. Because of the importance of gravity, we observe different characteristics with different orientations of the flow channels. Liquid water may fall away from the GDL and be pushed out with minimal effect on the local current density, accumulate on the GDL surface and cause local fluctuations, or become a pulsating flow of liquid slugs and cause periodic oscillations. We show that flooding in PEM fuel cells is gravity-dependent and the local current densities depend on dynamics of liquid slugs moving through the flow channels.* © 2008 American Institute of Chemical Engineers *AIChE J,* 54: 1313–1332, 2008
*Keywords: multi-phase flow, fuel cells, porous media, transport*

## Introduction

Perhaps the greatest challenge facing fuel cells is the difficulty in maintaining stable operation and control due to flooding by liquid water. The build up of water produced at the membrane/cathode interface is known to limit the current output from PEM fuel cells. To describe the effects of flooding, several models have been proposed.[1–6] Most of these hypothesize that liquid water condenses in the pores of the gas diffusion layer (GDL) creating a mass transfer resistance for oxygen to get to the membrane/electrode interface as illustrated in Figure 1.

Our group recently examined water permeation through the GDL and obtained results that contradicted the previous hypotheses about liquid flooding.[7] The GDL is a woven cloth or paper of carbon fibers that is usually treated with Teflon® to increase its hydrophobicity. We showed that water does not enter the GDL until a sufficient hydraulic pressure is applied to overcome the repulsive surface energy. The largest pores in the GDL are the first to permit water penetration, and once water penetrates the pores it can freely drain. Our results suggested a two-highway system for liquid and gas transport through the GDL, as illustrated in Figure 2. Liquid is driven by a hydraulic pressure from the membrane/cathode interface through the largest pores while gas moves from the gas flow channel to the membrane/cathode interface through smaller, but more plentiful, pores. Results that support these conclusions have also been reported using florescence microscopy to view the *ex-situ* transport of water through carbon paper.[8]

Recently, water intrusion has been used to determine the capillary pressure vs. liquid saturation curves for different GDL materials[9,10], providing pore volume distributions in these materials that are useful for design of new materials. The liquid breakthrough measurements are more useful to elucidate the rate of liquid water flow through the GDL. Only a few models have been published recently that account for preferential water flow through certain pores, even though this drastically changes the physics of how water is transported between the cathode catalyst layer and flow channel.[1–3,8]

This article contains supplementary material available via the Internet at http://www.interscience.wiley.com/jpages/0001-1541/suppmat

Correspondence concerning this article should be addressed to J. B. Benziger at benziger@princeton.edu.

© 2008 American Institute of Chemical Engineers

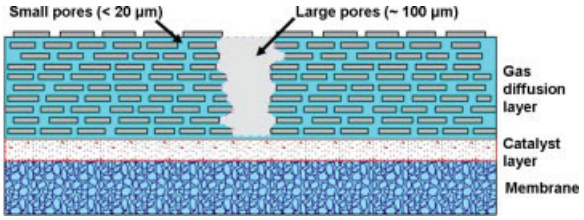


**Figure 1. Capillary condensation model of pore flooding in the GDL.**

This model assumes that liquid water condenses in the smallest pores of the GDL and sequentially fills the smallest pores and then the larger pores. When liquid water drops appear in the gas flow channel the entire GDL will be flooded. [Color figure can be viewed in the online issue, which is available at www.interscience.wiley.com.]

Liquid water has been observed to accumulate in gas flow channels, which has spawned the development of models for two-phase gas/liquid flow in the flow channels. Several researchers have built visualization fuel cells making use of neutron or optical imaging. Neutron imaging has been used to study water distribution in operating fuel cells, usually with serpentine channels and accumulation of water at the corners.[11–15] Optical imaging of transparent fuel cells has shown droplet growth and detachment, sometimes at preferential locations, or the formation of a film of liquid water.[16–21] Modeling efforts have focused on the transport of bulk water in the channels[22,23] or the conditions necessary to push liquid droplets along the surface of the GDL,[1,3,24,25] while others assumed the liquid droplets are suspended in the gas as a mist and carried out in the gas flow.[3] Another approach has been to build fuel cells with segmented electrodes to gain information about the current distribution over the active area of the MEA.[26–30] In one case, the flow channels were transparent so that condensation was observed in conjunction with distribution measurements.[28] Still, although it has been inferred that differences in the local currents are due to liquid water effects, direct correlations between liquid water build-up and dynamic current data has not been reported.

There is still little information available about how liquid in the flow channels affects the local current density in PEM fuel cells. In practice, engineers have circumvented the problem by increasing the gas flow rate until it is found sufficient to blow liquid out of the channels, decreasing the fuel utilization or adding the need for a recycling system. With the increased convection of water out of the cell, this usually creates the need for humidifiers for the feed streams. The result is a more costly and complex system. However, by thoroughly studying the operation of a simple fuel cell, we hope to gain insight into how systems can be more cleverly designed.

In this article, we will show that liquid water in the cathode flow channel is responsible for inhibiting mass transport to the membrane/cathode interface. We shall show how liquid water permeates through GDL media and forms liquid drops at the GDL/flow channel interface. Gravity or shearing action from the gas flow overcomes the surface adhesion of the drop to the pore, detaching the drop and allowing the water to move along the GDL surface. The drops accumulate and form slugs in the cathode gas flow channel. How and where this occurs in the cathode flow channel depends on the orientation of the fuel cell with respect to gravity. Altering the orientation and the direction of gas flows relative to gravity controls where liquid water accumulates and alters the local current in PEM fuel cells. Investigation of these effects has lead to observations of a variety of complex dynamic current outputs from a PEM fuel cell.

## Experimental

### *GDL permeation*

The flow through GDL media was tested in the cell illustrated in Figure 3 (a photo of the experiment setup is available in the supplementary material online as Figure 1S). A piece of GDL media 2.5 cm in diameter was mounted between two polycarbonate plates with 3 $cm^3$ plenums on either side of the GDL media. One plenum was connected to a beaker that acted as a liquid water reservoir. The beaker connected to the plenum with a Tygon® tube and could be raised or lowered to a desired elevation relative to the cell. The plenum on the other side had an inlet for a slow stream of nitrogen at the top and an outlet at the bottom with the effluent collected in a beaker on a scale. The gas side was imaged with a Sony IEEE-1394 CCD color camera with MVO double gauss macrolenses and interfaced to a computer through a LabVIEW program.

Before every experiment, the GDL media was dried by flowing nitrogen through both sides of the cell for 2 h. The water reservoir was hooked up with it sitting below the cell. The water reservoir was then raised to a desired height and held in position for 20 min, while recording the mass flow through the GDL media and obtaining video images of the water drops forming on the surface of the GDL. We tested Toray carbon paper and woven carbon cloth, both with 20% Teflon treatments and obtained from E-TEK (E-TEK Div. of De Nora N.A., NJ, USA).

### *Segmented anode fuel cell*

The fuel cell tests were done using the segmented anode parallel channel PEM fuel cell described elsewhere.[31] Briefly, the particular fuel cell used in the experiments presented here consisted of two polycarbonate plates with flow channels 1.6 mm wide × 3.2 mm deep × 75 mm long. The design was such that the anode and cathode flow channels were in a single plane and terminated in a 90° angle that

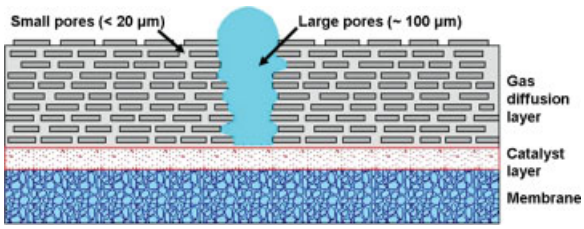


**Figure 2. Hydraulic driven flow model of liquid water flow in the GDL.**

The liquid water only enters the largest pores after the hydrophobic surface tension is overcome. The small pores remain unobstructed for gas transport. The small pores of the GDL only fill if the entire gas flow channel fills with liquid and the water pushes into the pores. [Color figure can be viewed in the online issue, which is available at www.interscience.wiley.com.]

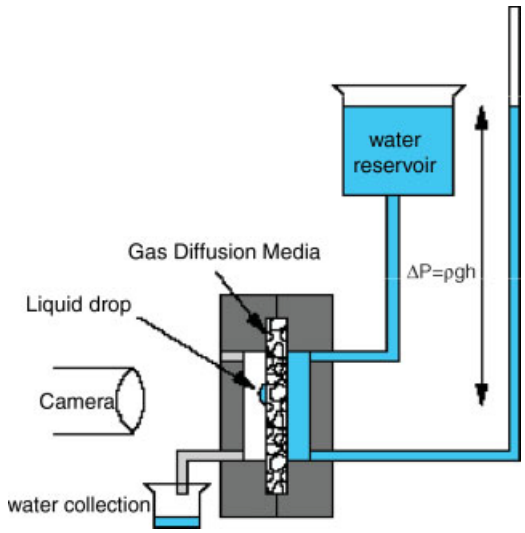


**Figure 3. Schematic of the cell for measuring and visualizing flow through GDL media.**

[Color figure can be viewed in the online issue, which is available at www.interscience.wiley.com.]

connected into a tube fitting adapted to 1/8″ polyethylene tubing. Two stainless steel electrodes, 6.4 mm wide × 54 mm long, lined the cathode flow channel. The anode consisted of six segments of stainless steel, 6.4 mm long and separated by 3.2 mm along the channel. The lead wires from each anode segment were connected individually to a 0.1-Ω sensing resistor, $R_{sense}$. The six leads from the sensing resistors at the anode were connected together, and the common lead was connected through a 0–20 Ω, 10-turn potentiometer to the cathode, as diagramed in Figure 4 (a photo of the experiment setup is available in the supplementary material online as Figure 2S). We operated with the load resistance > 0.5 Ω. The sensing resistors were a total resistance of 0.016 Ω so they contributed <3% of the total external impedance. A CCD camera was positioned to view the cathode flow channel (we could also look at the anode flow channel, but all the interesting phenomena were observed at the cathode). Video images were collected and time stamped so that they could be correlated with the current and voltage measurements.

A computer DAQ board, interfaced through LabVIEW, read the voltage drops across the potentiometer (that served as the load resistance) and those across each of the sensing resistors. Data samples were read from the board at 20 Hz and then conditioned to mitigate the noise in the measurements. When data was being saved to a file at 1 data set per second, each input was sampled and 16 values were averaged. For longer term experiments, 1024 samples were read from the board, averaged, and written to the file at 1 data set per minute. With this, the fluctuations in the data from noise were kept acceptably low at no more than ±0.0001 A.

The tubing from the gas flow channel outlets was bent down and bled into 10 mL graduated cylinders with a small hydrostatic head (~2–3 cm $H_2O$), so that the cell pressure was effectively 1 bar. Liquid in the cylinders kept air from back diffusing into the flow channels; we were able to measure the total liquid water leaving from both the anode and cathode. It was also possible to see gas bubbles leaving the anode and the cathode, which helped to identify the extent of reactant conversion in the fuel cell. This setup allowed for the flows at the anode and cathode to be either co-current or counter-current. All the results reported here are for fuel cell operation at 20–25°C; the vapor pressure of water is sufficiently low (~0.025 bar) so that convection of water vapor is negligible and almost all the water transport is by liquid flow.

The MEA was constructed in the lab from a Nafion 115 membrane, carbon cloth GDLs, and silicon gaskets. The GDLs were ELAT V2.1 obtained from E-TEK with the catalyst, 0.5 mg/cm$^2$ of 20% platinum on Vulcan XC-72, applied to one side. The dimensions of the electrodes were 5.72 cm long by 1.43 cm wide to give a total area of 8.17 cm$^2$ (only 10%, 0.91 cm$^2$, of the MEA is exposed to the gas channel, the other 90% of the MEA is under the stainless steel electrodes).

### *Fuel cell operation*

Hydrogen and oxygen were supplied from commercial cylinders through mass flow controllers at flow rates of 1–20 standard cubic centimeters per minute (sccm). The computer DAQ system was used to control and read the gas flow rates. There were also relative humidity sensors placed in the outlets from the gas flow channels and the RH could be logged. In the experiments reported here the liquid water was always present in the flow channels and the relative humidities in both the anode and cathode outlets were always 100%.

Most of the experiments were done with fixed flow rates of 6 sccm $H_2$ and 3 sccm $O_2$, or 12 sccm $H_2$ and 6 sccm $O_2$. Through a series of tests, we observed that with a load resistance of 0.5 Ω and flow rates less than 6 sccm $H_2$ and 3 sccm $O_2$, no gas bubbles were seen from the outlets of the anode and cathode. This indicated that all of the gas was consumed by the reaction, commonly referred to as a stoichiometry ($\xi$) of 1, where $\xi$ is the ratio of gas supplied through the feed to

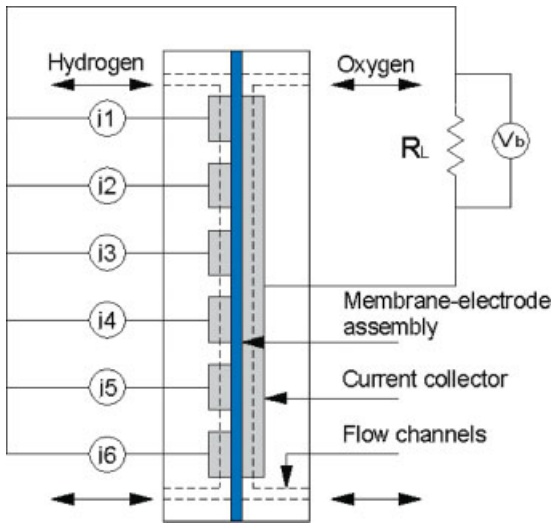


**Figure 4. Diagram of electrical connections for the SAPC fuel cell.**

The six segments of the anode are connected in parallel such that the total current goes through an external load resistance and then to the cathode. [Color figure can be viewed in the online issue, which is available at www.interscience.wiley.com.]

that consumed by the fuel cell with the given current. When we increased the flow rates to 7 sccm $H_2$ and 3.5 sccm $O_2$ or greater, gas bubbles were seen from the outlets of the anode and cathode. We will refer to the inlet flow rates of 6 sccm $H_2$ and 3 sccm $O_2$ as $\xi_1$, and 12 sccm $H_2$ and 6 sccm $O_2$ as $\xi_2$. The maximum total current from the SAPC fuel cell driving a 0.5 Ω load impedance at 25°C and 1 bar total pressure was ~0.8–0.9 A. We found a variability in the internal resistance of about 10% from MEA to MEA, corresponding to a variability in the total current. The flow rates corresponding to $\xi_1$ limit the maximum current to 0.8 A with complete conversion of the reactants. Increasing the reactant feed rate beyond $\xi_1$ did not result in any substantial increase in the maximum total current from the SAPC fuel cell. Although it has been reported that severe degradation of the catalyst can occur under starved conditions,[32–34] we did not observe any effects through consecutive experiments with the same MEA. We have also run an autohumidified self-draining fuel cell under anode starved conditions for >1000 h with negligible change in the MEA performance.[35] This is perhaps due to the choice to let the fuel cell run autonomously under a constant load resistance without the addition of potentiostatic or galvanostatic controllers. Future work will investigate this further.

The experiments summarized here consist of a vast array of data. A typical data set consists of the six current measurements for the six anode segments, the voltage drop across the load, anode and cathode flow rates, and the relative humidity in the anode and cathode effluent. This data is recorded with a time stamp at a frequency of between 0.1 and 1 Hz and stored as a data array. A typical experiment runs from 15,000 to 172,800 s. It is impossible to summarize all the information contained in experiments in a few simple graphs. We have chosen to highlight certain features of the data. A database of excel files containing the data from all our vetted data (currently consisting of ~100 files with average size 20 MB) are available at our web site (http://pemfc.princeton.edu/data.html). Video images were selectively recorded at various times during operation. The video images are time stamped and can be correlated with the Excel data files. The video images are also available.

## Results

### *Flow through GDL media*

No liquid water flows through the GDL media until a critical hydrostatic pressure head is applied by raising the water reservoir to an appropriate height. The required pressure head was 15–17 cm $H_2O$ for the carbon cloth and 60–80 cm $H_2O$ for the Toray paper, or 1500–1700 Pa and 5900–7800 Pa, respectively. These value are at the low range of those reported in work investigating the capillary pressure-saturation relation for different GDL materials.[9,10] This is expected with our setup since pressure does not continue to build up enough to break through the smaller pores once water begins to flow through the largest pores. Once the critical hydrostatic head is exceeded, a continuous path of liquid water is established through the largest pores in the GDL media and liquid flow commences with the water freely draining under the applied hydrostatic head. This occurs through a few water drops (1–4) forming on the surface of the GDL. The drops grow to a critical size, fall by gravity to the bottom of the plenum, and then drain from the cell. The process repeats itself with the water drops always forming at the same locations. Figure 5 is a series of photos showing drops growing and the process repeating for the carbon cloth. The critical hydrostatic pressure head to initiate flow and the measured water flow rate for the first 2–3 min after flow started are summarized in Table 1. Also given in Table 1 is the critical radius for the drop before it falls by gravity, as determined from the videos. The key results from these studies are that liquid flow is carried through a small number of the largest pores in the GDL. The Toray paper has smaller pores than carbon cloth so the critical pressure to initiate flow is greater and the flow through the smaller pores is less.

### *Fuel cell operation*

The data from the SAPC fuel cell are complex and not easily summarized. We will focus here on the general trends associated with changing cell orientation, flow rate, and flow direction. It is also possible with our setup to switch between co- and counter-current flow and change the temperature of the fuel cell. In the work reported here, we will focus on co-current operation at room temperature. The reader is referred to Benziger et al.[31] for a thorough discussion of co- vs. counter-current flow with the SAPC fuel cell.

All of the experiments were done with a fixed load at 25°C. We focused on two sets of flow rates, $\xi_1$ (6 sccm $H_2$, 3 sccm $O_2$) and $\xi_2$ (12 sccm $H_2$, 6 sccm $O_2$). There are five different physical orientations (three horizontal and two vertical) of the SAPC PEM fuel cell which are defined by the effect that gravity has on liquid accumulation in the gas flow channel. For this relatively simple fuel cell with a very lim-

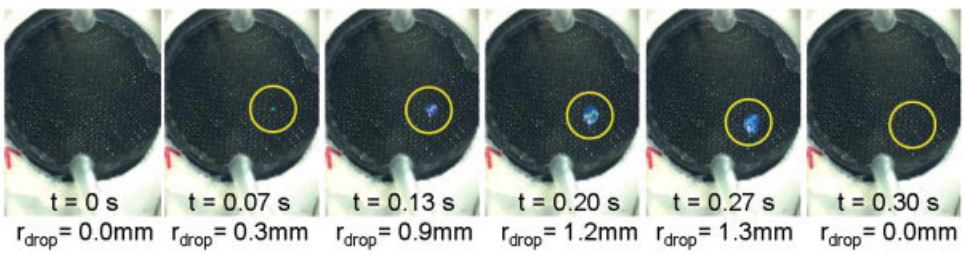


**Figure 5. Series of photos showing drop formation and detachment from the surface of a carbon cloth GDL under an applied hydraulic pressure of 170 mm $H_2O$.**

[Color figure can be viewed in the online issue, which is available at www.interscience.wiley.com.]

**Table 1. Water Permeation Through GDL Media**

| GDL Media | Required Head for Water Permeation (mm $H_2O$) | Water Permeation Rate at Critical Hydraulic Pressure (g/min) | Critical Drop Radius for Detachment ($\mu$m) | Critical Pore Radius Based on Initial Drop Formation ($\mu$m) |
|---|---|---|---|---|
| 20% Teflon-treated cloth | 170 | 1.2 | 1,250 | 140 |
| 20% Teflon-treated toray paper | 600 | 0.22 | 600 | 21 |

ited set of operating parameters (only one load, only one temperature and two sets of flow rates) there are 20 different experimental systems under investigation. Of these 20, only two can be characterized as having stable (time invariant) steady states. The other 18 configurations give rise to complex spatio-temporal patterns of current density. All the experimental systems have been examined multiple times. The results presented in this article are representative, but the reader is referred to the data files available on our website to see the full extent of spatio-temporal current density patterns.

The total area of each of the fuel cell flow channels is 1.2 $cm^2$ with a volume of 0.38 $cm^3$. The maximum current obtained with our membrane-electrode-assemblies was 0.85–0.9 A (current density of 0.94–0.99 $A/cm^2$, based on the exposed MEA surface in the flow channels) with an external load of 0.5 Ω. At a current of 0.9 A, the time for liquid water to fill the cathode flow channel is 4000 s. All tests have been run for periods that last more than 10,000 s to make sure the liquid content in the flow channel has had time to equilibrate.

We will present the data in three formats. The most general presentation will be the currents in each electrode segment as a function of time. This consists of a set of line graphs, often truncated to represent a limited time period. Many of the experiments ran for over 100,000 s and the local current variations occur on time scales from 1 to $10^4$ s; time slices are chosen to highlight specific characteristics of the current density patterns. These figures also show the inlet flow rates to the anode and cathode so it is possible to associate changes in the spatio-temporal current patterns with changes in flow. A second presentation of the data is the current profiles along the length of the flow channel. Because of the time-varying nature of the current density, these would typically be snap shots at a fixed moment in time. We have represented the current profiles as steady-state with error bars to denote the time-varying component. The third type of data presentation is a correlation of current density as a function of time along with a photographic sequence of water within the flow channel. The data collected from the SAPC fuel cell are much different than conventional I–V data reported for fuel cells, and the massive amount of information must be studied to fully understand its presentation. The reader is always welcome to view the raw data.

### *Horizontal configuration*

Three different horizontal configurations of the SAPC PEM fuel cell are possible. They are defined by the effect that gravity has on liquid accumulation in the gas flow channel. Illustrated in Figures 6 and 7 are two of the horizontal configurations: (i) the cathode below the anode so that liquid water at the cathode falls away from the GDL by gravity; (ii) the cathode above the anode such that liquid water accumulates on the surface of the GDL. The third horizontal configuration, (iii), is with the anode and cathode in the same horizontal plane such that liquid water accumulating in the cathode flow channel will fall onto the side walls of the channel and only partially block oxygen access to the GDL. The results from the experiments with configuration H-iii were qualitatively the same as those with configuration H-i, and so will not be discussed further. With each configuration, the fuel cell was operated with the load impedance fixed at 0.5 Ω, dry $H_2$ and $O_2$ feeds, and at a temperature of 25°C. By convention we define electrode segment 1 as that nearest the oxygen inlet. For co-current flow, as with the data presented here, the hydrogen feed is also at electrode segment 1. During operation, the feed flow rates were adjusted while the current and the voltage measurements continued to be recorded. Visual observations of any liquid water in the anode and cathode were intermittently recorded. Video clips were recorded of liquid water motion in the cathode flow channel during "steady-state" operation. The steady-state results from these tests are summarized in Table 2. A summary of all the tests conducted for this study is provided in the Appendix. The data files have been made available at the web-site (http://pemfc.princeton.edu/data.html).

### *Horizontal configuration: cathode down*

The temporal currents in all the electrode segments at stoichiometry $\xi_1$ and $\xi_2$ for configuration H-i are shown in Figure 8. It is evident that the currents show no fluctuations for 20,000 s at the higher stoichiometry of $\xi_2$. Gas bubbles were seen leaving the outlet tubes at both the anode and cathode, and the relative humidity of the gas effluents was 100%. Collection of the liquid water pushed out of the outlets showed greater than 90% recovery of the water produced by the fuel cell reaction, with the rest taken up by the membrane, trapped in parts of the GDLs and flow channels, or

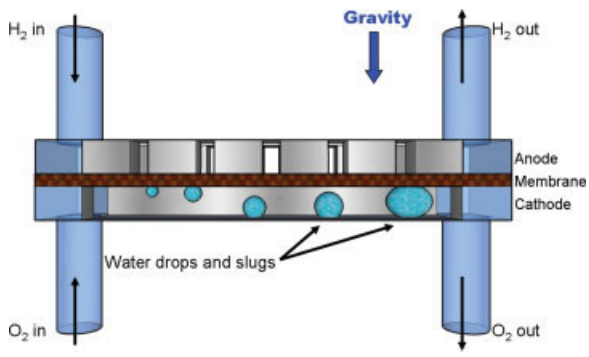


**Figure 6. Schematic of the horizontal fuel cell with the cathode facing down (H-i).**

Droplets grow on the GDL until they detach and fall to the back of the channel. The droplets continue to grow as they are pushed along the channel. [Color figure can be viewed in the online issue, which is available at www.interscience.wiley.com.]

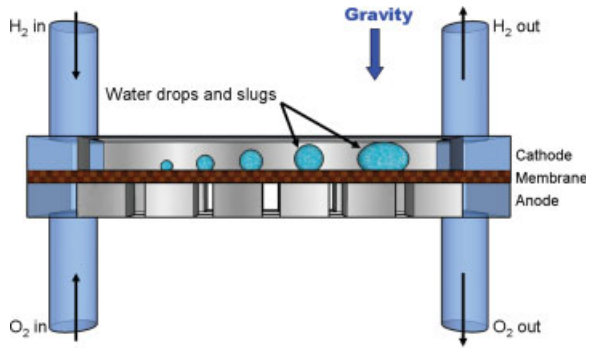


**Figure 7. Schematic of the horizontal fuel cell with the cathode facing up (H-ii).**

Droplets sit on top of the GDL and grow as they are pushed along the channel. [Color figure can be viewed in the online issue, which is available at www.interscience.wiley.com.]

carried off as water vapor in the anode and cathode effluents. Furthermore, it was possible to routinely run the SAPC fuel cell in this configuration indefinitely with stable operation.

When the flow rates are reduced to $\xi_1$, the electrode currents immediately begin to show significant local current fluctuations, with the largest fluctuations seen at the electrode segments furthest downstream. These erratic fluctuations persisted indefinitely. Observations of the cathode flow channel showed that a liquid water slug was blocking the end of the channel when the current in segment 6 was low. When the slug was pushed into the effluent tube, the current increased. No gas bubbles were observed from the outlet tubes of the anode and the cathode, indicating that all the feeds were consumed. The distribution of the current along the flow channel also shows a significant change with the flow reduction. The currents decrease in electrode segments 5 and 6, as expected, because of depletion of the reactants downstream in the flow channel. The surprising result is that the currents increase in segments 1 and 2 near the inlet to the flow channel. The response to the change in the inlet flow rate occurred almost immediately and was reversible. This suggests that these changes in current distribution were produced from local variations in concentrations of hydrogen and oxygen and were not directly related to local water content in the GDL or membrane. In-plane currents resulting from local variations in a fuel cell system have been observed in the bipolar plates of fuel cells stacks[36,37] and in a cell with segmented electrodes that were connected through a bipolar plate.[38] The large redistribution we observed was not expected in our cell, though, because the segments are electrically isolated except through the GDL.

### *Horizontal configuration: cathode up*

Flipping the fuel cell so that the cathode faced up, configuration H-ii, resulted in distinctly different behavior. In contrast to the stable currents with a stoichiometric excess of the feeds, as was observed for H-i, the local current densities for H-ii show fluctuations at both low and high stoichiometries, $\xi_1$ and $\xi_2$. Shown in Figure 9 are the spatio-temporal current data for configuration H-ii. With $\xi_2$, corresponding to the time period 5000–80,000 s in Figure 9, the currents in every electrode segment show fluctuations. The fluctuations resemble regular square wave oscillations with time periods of about 3000–4000 s and are most pronounced in segments 4, 5, and 6. In some runs, the amplitude of the oscillations grew with time or only occurred in the current from segment 6. Water droplets were observed to form on top of the GDL, close to the oxygen inlet where the current density was the highest. Figure 10 shows one such image, corresponding to a time of 80,674 s in Figure 9. The droplets grow to a critical size, at which point they detach, are pushed along the GDL, and coalesce with other droplets until they form a slug that spans the channel. This blocks the flow of oxygen to the segments closer to the outlet and causes the instabilities both up- and down-stream of the slug.

The current density profile at $\xi_2$ for H-ii is slightly different than for H-i, as shown in Figure 11. Comparing the profiles gives more evidence of the importance of gravity with flooding in the flow channels. The current increases from electrode segments 1 to 3 for both configurations of the fuel cell. When the cathode is facing down, the current increases sharply upstream and then levels off downstream at segments 4, 5, and 6; however, in comparison, when the cathode faces up the current is significantly lower downstream in segments 3 through 6. When the flow rates were increased from $\xi_1$ to $\xi_2$, the current profile redistributed along the channel for both configurations. At the higher flow rate, $\xi_2$, the current was lowest at segment 1 and continuously increased to be highest at segment 6 for both configurations. With the cathode down, the currents in all segments lined out to stable steady-state values after the flow rate was increased to $\xi_2$. In contrast, with the cathode up, configuration H-ii, a second current redistribution occurred after about 1300 s after increasing the flow rate to $\xi_2$ and took about 10,200 s to reach the oscillating "steady-state" evident in Figure 8. The oscillating current profiles for configuration H-ii were qualitatively similar for $\xi_1$ and $\xi_2$, but the magnitude of the current fluctuations were larger at the lower stoichiometry. As there was excess of fuel at $\xi_2$, it must be the case the liquid water in the flow channel was collecting

**Table 2. Summary of Horizontal Fuel Cell Operation**

| | | | Segment Current (mA) Position 1 is the Cathode Inlet | | | | | | |
|---|---|---|---|---|---|---|---|---|---|
| Configuration | $T$ (°C) | $\xi$* | 1 | 2 | 3 | 4 | 5 | 6 | $\Delta V_{load}$ |
| (i) Co-current | 25 | 1 | 146 | 179 | 158 | 160 | 90 | 61 | 0.446 |
| (ii) Co-current | 25 | 1 | 160 | 203 | 180 | 131 | 64 | 40 | 0.388 |
| (i) Co-current | 25 | 2 | 124 | 151 | 146 | 180 | 166 | 173 | 0.525 |
| (ii) Co-current | 25 | 2 | 118 | 158 | 170 | 175 | 142 | 140 | 0.455 |
| (i) Counter-current | 25 | 1 | 87 | 126 | 159 | 182 | 129 | 107 | 0.383 |
| (ii) Counter-current | 25 | 1 | 194 | 138 | 124 | 70 | 30 | 17 | 0.287 |
| (i) Counter-current | 25 | 2 | 80 | 114 | 148 | 186 | 154 | 145 | 0.415 |
| (ii) Counter-current | 25 | 2 | 90 | 122 | 134 | 185 | 167 | 164 | 0.430 |

*$\xi$ = 1 corresponds to $F_{H2}$ = 6 sccm/$F_{O2}$ = 3 sccm, $\xi$ = 2 corresponds to $F_{H2}$ = 12 sccm/$F_{O2}$ = 6 sccm.

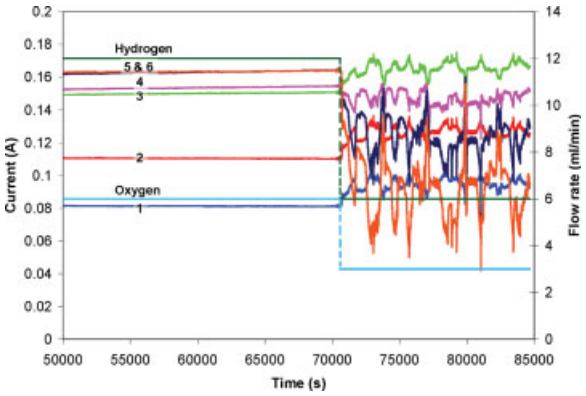


**Figure 8. Spatio-temporal current profiles for the SAPC fuel cell in the horizontal configuration with the cathode down (H-i).**

"Steady-states" are shown with both $\xi_1$ (fluctuating) and $\xi_2$ (stable). The feed flow rates were decreased at 70,000 s, leading to the large fluctuations in the current. The electrode segment is indicated by number with the oxygen inlet upstream of segment 1 (Filename: MEA-5-25-constcnt-flooding-cathodedown2). [Color figure can be viewed in the online issue, which is available at www.interscience.wiley.com.]

on top of the GDL close to the outlets. When water is produced at the catalyst layer, it flows through the largest pores to the flow channel, leaving smaller pores open for gas flow. However, when water is already in the flow channel and droplets are pushed along the GDL, the water blocks all of the pores and creates a much greater resistance for the mass transfer of oxygen to the catalyst.

The dynamic response was also examined when the reactant flows were reduced from $\xi_2$ to $\xi_1$ with both configurations. With H-ii, as the liquid water had already caused a large redistribution and fluctuations in the local currents, the flow reduction does not qualitatively change the current profile. The most notable change is an increase in the magnitude of the fluctuations, as seen by the larger error bars for H-ii and $\xi_1$ in Figure 11. For H-i, erratic fluctuations followed a

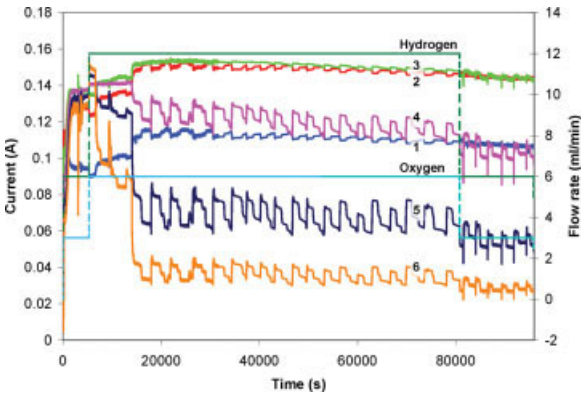


**Figure 9. Spatio-temporal current profiles and feed flow rates for the SAPC fuel cell in the horizontal configuration with the cathode facing up (H-ii).**

Oscillations with periods of 3000–4000 s are seen with the greatest magnitude in the segments closest to the outlets. The electrode segment is indicated by number with the oxygen inlet upstream of segment 1 (Filename: MEA5-25-constco-flooding-cathodeup3). [Color figure can be viewed in the online issue, which is available at www.interscience. wiley.com.]

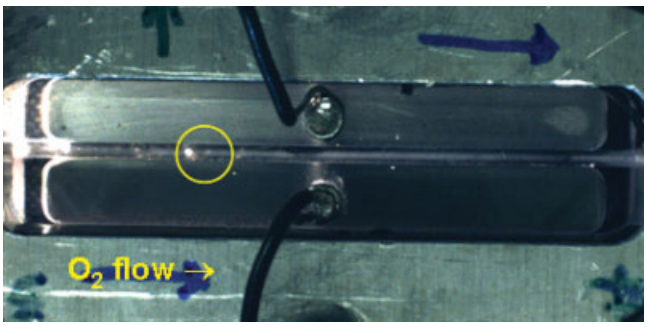


**Figure 10. Photo of SAPC fuel cell in the H-ii orientation corresponding to time 80,674 s in Figure 7.**

Droplets are seen forming and sitting on top of the GDL. [Color figure can be viewed in the online issue, which is available at www.interscience.wiley.com.]

redistribution in the currents with the decrease in reactant flows, as seen in Figure 8 and highlighted by the large error bars in Figure 11. The decrease in the local currents in the downstream section of the fuel cell is less with configuration H-i due to the assistance from gravity in removing liquid water from the cathode flow channel.

Comparing the two different fuel cell configurations indicates that gravity-assisted drainage of liquid from the cathode gas flow channel was the key difference. When water drainage is assisted by gravity and there is a stoichiometric excess of reactant feed, the fuel cell operates stably. When the reactant feed is reduced to the point where water slugs build up in the cathode flow channel the local current density fluctuates because the water in the flow channel blocks reactants from getting to the membrane/electrode interface. The current distributions for the two horizontal flow configurations

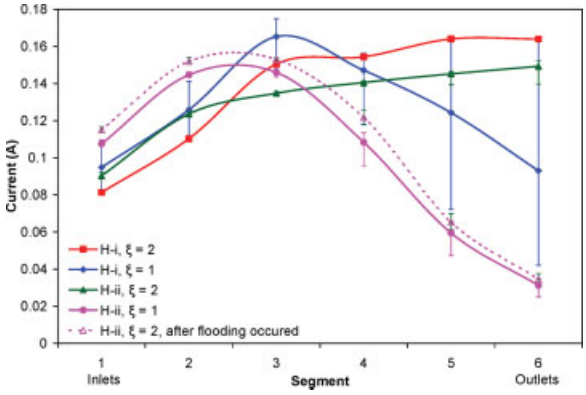


**Figure 11. Steady-state current density profiles for the SAPC $H_2/O_2$ fuel cell in two horizontal configurations: the cathode facing down (H-i) and the cathode facing up (H-ii); and two feed stoichiometries: $\xi_1$ and $\xi_2$.**

The oxygen inlet is always upstream of electrode segment 1. With $\xi_2$, the currents are high all along the channel before flooding occurs. After flooding, the local currents are slightly higher toward the inlets and dramatically lower closer to the outlets. The same trends are observed with $\xi_1$. The error bars represent the fluctuations in the current. [Color figure can be viewed in the online issue, which is available at www.interscience.wiley.com.]

**Table 3. Summary of Vertical Fuel Cell Operation**

| | | | Segment Current (mA) Position 1 is the Cathode Inlet | | | | | | |
|---|---|---|---|---|---|---|---|---|---|
| Configuration | $T$ (°C) | $\xi$* | 1 | 2 | 3 | 4 | 5 | 6 | $\Delta V_{load}$ |
| (i) Co-current | 25 | 1 | 87 | 121 | 129 | 143 | 121 | 93 | 0.388 |
| (ii) Co-current | 25 | 1 | 193 | 242 | 200 | 86 | 29 | 17 | 0.432 |
| (ii) Counter-current | 25 | 1 | 145 | 156 | 197 | 153 | 98 | 54 | 0.448 |
| (i) Co-current | 25 | 2 | 86 | 120 | 129 | 147 | 132 | 106 | 0.407 |
| (ii) Co-current | 25 | 2 | 116 | 161 | 173 | 170 | 144 | 147 | 0.520 |
| (ii) Counter-current | 25 | 2 | 173 | 164 | 163 | 152 | 107 | 79 | 0.476 |

*$\xi$ = 1 corresponds to $F_{H2}$ = 6 sccm/$F_{O2}$ = 3 sccm, $\xi$ = 2 corresponds to $F_{H2}$ = 12 sccm/$F_{O2}$ = 6 sccm.

discussed are summarized in Table 2. These are time-averaged currents over periods of 5000–10,000 s. Included in Table 2 is data for the same configurations, but with counter-current flows. The currents tend to be higher toward the middle of the channel when the flows are counter-current, but the same effects from flooding are still evident.

### *Vertical configuration*

Two distinct vertical configurations of the SAPC fuel cell were examined based on the direction of gas flow at the cathode relative to gravity. The cathode flow could be in the direction of gravity, configuration V-i, or it could be against gravity, configuration V-ii. When the cathode flows are in the direction of gravity, water drainage is gravity-assisted. Oxygen flow counter to gravity requires the gas to lift the liquid up the channel for it to be removed from the cell. Counter-current flows were examined, but yielded qualitatively similar results; data for counter-current flows are available on our website. The same set of operating conditions was used as for the horizontal flow: a load impedance of 0.5 Ω, flow rates with stoichiometry $\xi_1$ or $\xi_2$, and a temperature of 25°C. Table 3 summarizes the time-averaged "steady-state" current profiles for the six different tests for the vertically oriented SAPC fuel cell [data for counter-current flow, with the oxygen flow against gravity (configuration V-ii) has also been included in Table 3].

### *Vertical configuration: gas flow with gravity*

The flow of liquid water with the vertical SAPC fuel cell was analogous to that seen with the liquid water flow through the GDL, shown in Figure 5. Liquid drops were observed to consistently form at a single location in the cathode flow channel. The drops grew until they nearly spanned the flow channel, then detached and fell rapidly down the length of the flow channel. When the gas flow in the cathode was downward, in configuration V-i, this process repeated itself with a frequency of ~100 s. There were small fluctuations in the current from the segment nearest to where the drop formed; the current would decrease by 5–10% while the drop was forming and then rise after the drop fell. The currents in the segments distant from where the drop formed appeared to be quite stable.

### *Vertical configuration: gas flow opposing gravity*

The current densities for the vertical SAPC fuel cell with co-current flows going against gravity, configuration V-ii, are much more complex in nature. The current density profiles do not appear to be described by simple deterministic models; for the same set of operating conditions the current density could be stable, show regular periodic oscillations or show random fluctuations. All types of behaviors were observed in multiple studies. We found ways to induce periodic oscillations in the current density, but we could not shutdown and restart the fuel cell and guarantee that we could restore it to the same state of operation!

Figures 12 and 13 show one example of how the current profile can evolve throughout the course of an experiment with configuration V-ii. Figure 12 tracks the current density in the SAPC fuel cell as a function of time after the feed flow rates are reduced from $\xi_2$ to $\xi_1$. At the high flow rates, the currents in each segment are stable. Liquid was seen to accumulate in the cathode flow channel just below the active area of the MEA and periodically a liquid slug rose rapidly through the flow channel. The slugs were ~10 mm long and rose up the channel at a frequency of one slug every 10–12 s. They traveled through the column in 1 s, approximately equal to the gas velocity in the cathode.

When the gas flow rate is reduced from $\xi_2$ to $\xi_1$, the current redistributes as seen previously with the horizontal configurations. The current density increases near the gas inlet and decreases downstream of the inlets. Fluctuations in the current

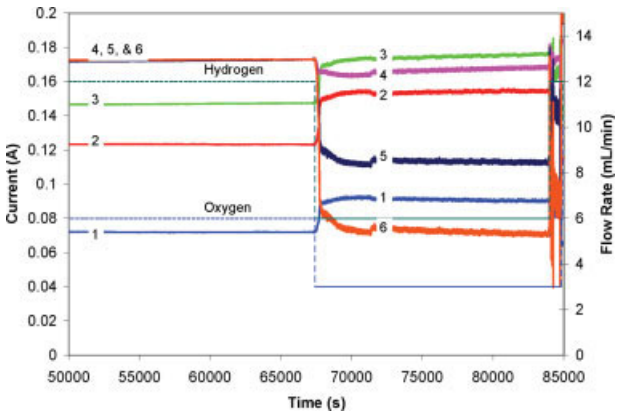


**Figure 12. Spatio-temporal current profiles and feed flow rates for the SAPC fuel cell in a vertical orientation with flows upward.**

The flow rates were changed at 67,500 s, which resulted in a redistribution of the current. At 84,000 s, the inlet flow rate at the anode was increased while the cathode flow rate was kept constant. The electrode segment is indicated by number with the oxygen inlet upstream of segment 1. A blowup of the current distribution after the flow rate change at 84,000 s is shown in Figure 13 (Filename: MEA5-25-constco-flooding-inletsdown6). [Color figure can be viewed in the online issue, which is available at www.interscience.wiley.com.]

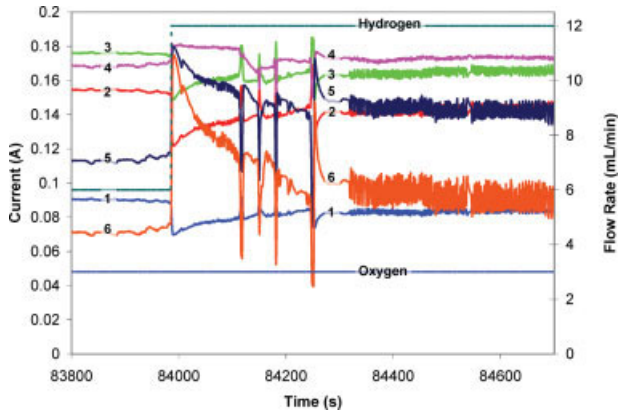


**Figure 13. Blow up of the current response of the vertical SAPC fuel cell with the gas flows rising against gravity.**

At 84,000 s the inlet flow rates were changed from $\xi_1$ for both the hydrogen and oxygen feeds to $\xi_1$ for oxygen and $\xi_2$ for hydrogen. The electrode segment is indicated by number with the oxygen inlet upstream of segment 1 (Filename: MEA5-25-constco-flooding-inletsdown6). [Color figure can be viewed in the online issue, which is available at www.interscience.wiley.com.]

densities also started with the reduced flow. After increasing only the anode flow to $\xi_2$ at 84,000 s, the stability of the currents changes dramatically as shown in Figure 13. We were not expecting to see any change in the current distribution and stability because the oxygen flow at the cathode was still fixed, but instead increasing the anode flow appeared to induce large fluctuations in the currents. Figure 13 shows that the current takes about 350 s to move to a steady-state, with very large fluctuations in the current over that time period. The new "steady-state" is periodic oscillations at the downstream electrode segments located at the top of the flow channels.

### *Vertical configuration: effect of reactant flow rate*

In most cases with the V-ii configuration, stable current density profiles were found at higher gas flow rates, where both hydrogen and oxygen were fed in stoichiometric excess of the current. If the auto-humidified SAPC fuel cell current was allowed to self-ignite with inlet flow rates of 7 sccm $< F_{H2} <$ 20 sccm, 3.5 sccm $< F_{O2} <$ 12 sccm, the SAPC fuel cell would line out with a stable current density profile. Gas bubbles were seen exiting from both the anode and cathode going into water reservoirs. Liquid slugs of volume 2–3 $\mu$L were also seen in the tube from the exit of the cathode. They were pushed through the tube with the excess oxygen to be collected in the water reservoir. For inlet flow rates of $F_{H2} \leq$ 6 sccm and $F_{O2} \leq 3$ sccm, the reactants were completely reacted to water in the fuel cell. No gas bubbles were seen to exit from either the anode or cathode when the $H_2/O_2$ feed ratio was 2; if one reactant was in excess, gas bubbles were observed. At the low inlet flow rates different patterns of current density and liquid movement were observed. If the inlet flow rates were reduced below $F_{H2} = 6$ sccm and $F_{O2} = 3$ sccm, and we waited for sufficient time (this could be as long as 100,000 s in some cases), the system would eventually evolve to a cathode flow channel partially flooded by slugs at the bottom. The liquid slugs would grow at the bottom and periodically be pushed up through the flow channel. This would result in current oscillations.

The current profiles for co-current flows at $\xi_1$ and $\xi_2$ are shown in Figure 14. These current density profiles are similar to those seen with horizontal flows. The most distinguishing feature is the large decrease in current downstream of the inlet for $\xi_1$. Liquid slugs in the flow channel appear to have exacerbated the starvation of the reactants to the downstream electrode segments. The error bars seen for $\xi_1$ show the magnitude of the oscillations.

In some cases, the oscillatory behavior began immediately after a flow reduction to $\xi = 1$; however, it was not a deterministic process. In one case, the oscillations began only after the oxygen flow was decreased to 1.5 sccm, or $\xi = 0.5$. The fuel cell was allowed to self-ignite and equilibrate with flows of 7 and 3.5, just above $\xi = 1$. After about 14 h with stable operation, the $H_2$ flow was increased to 12 sccm so that starvation at the anode was not a factor, and the $O_2$ flow was decreased by 0.5 sccm every 5000 s. Surprisingly, the currents remained stable with only small irregular fluctuations until the $O_2$ flow was reduced to 1.5 sccm at 111,400 s. The current profile leveled off for about 1000 s after the initial decrease in total current. Then, at 112,400 s, the currents spontaneously began to oscillate, as shown in Figure 15 (the spatio-temporal data showing each flow decrease can be found in Figure 3S in the supplementary material available online). As the local current densities close to the inlets dropped, those closer to the outlets rose, so that the average total current remained about constant. The oscillations persisted for the duration of the experiment, about 2000 s, with a period of 5 s.

With the fuel cell starved, the effects of the slug motion were most prominent near the inlets. Figure 16 shows the detail of the current oscillations along with images of the cathode flow channel from a video that we captured. The

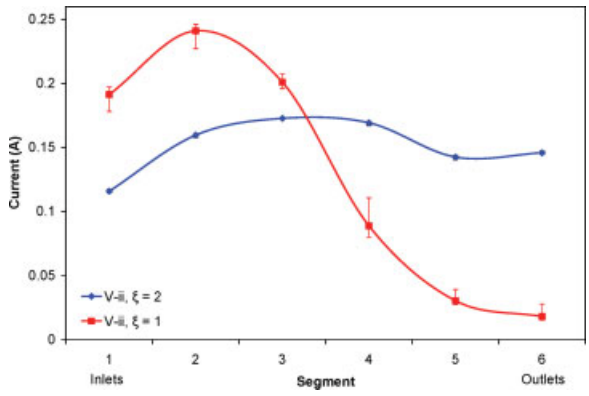


**Figure 14. Steady-state current density profiles for the vertical SAPC fuel cell with the flows against gravity (V-ii) and two different feed stoichiometries: $\xi_1$ and $\xi_2$.**

The oxygen inlet is always upstream of electrode segment 1. With $\xi_2$, the currents are high all along the channel with only small deviations from segment to segment. With $\xi_1$, the currents are higher toward the inlets and dramatically lower toward the outlets due to liquid water exacerbating the starvation effects. The error bars represent the fluctuations in the current. [Color figure can be viewed in the online issue, which is available at www.interscience.wiley.com.]

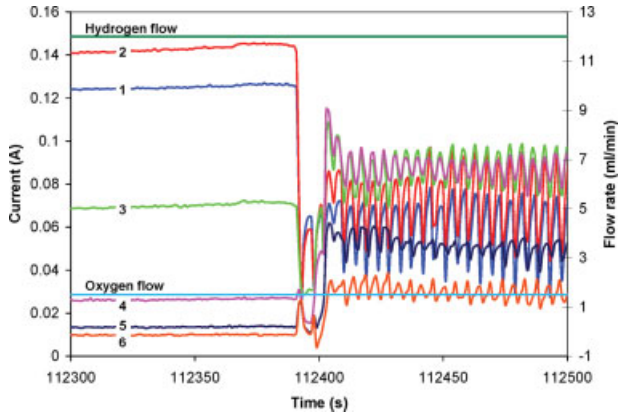


**Figure 15. Spatio-temporal current profiles with the vertical SAPC in vertical configuration V-ii.**

The flows were run just above $\xi_1$ for 50,000 s with only small fluctuations in the currents. At 83,000 s, the oxygen flow started being reduced until regular periodic oscillations started at about 112,400 s. The currents redistribute with those near the inlets dropping dramatically, while those closer to the inlets increase. The electrode segment is indicated by number with the oxygen inlet upstream of segment 1 (Filename: MEA5-25-constcoflooding-inlets-down9). [Color figure can be viewed in the online issue, which is available at www.interscience.wiley.com.]

oscillations correlate very well with the movement of the water slugs in the channel. New slugs form around the middle of segment 1, blocking the flow of oxygen and causing the currents to drop by as much as 70%! As the slug is pushed up the channel, the gas begins to break through the slug and water falls back down the channel. The currents recover in the lower segments as oxygen is blocked from reaching the higher segments. For the same reason, small drops in the currents are seen from the segments close to the outlets. The water falling back down the flow channel combines with droplets emerging from the GDL to form a new slug in the same location and the oscillations continue.

Figures 8, 9, and 12 all show different "steady-state" spatio-temporal current profiles in the SAPC fuel cell operated at the same conditions. We have seen several different current profiles but that all appear to be variations of the three basic types shown earlier. The currents are either steady, show regular oscillations that correlate with the periodic formation and movement of slugs, or fluctuate randomly with random slug movement. We have carried out more than 25 tests for the SAPC fuel cell in the vertical orientation (corresponding to over 1000 h of testing) and we have not been able to identify any operating trajectory that leads to a specific spatio-temporal current profile. We have found that by reducing the inlet flow rates it is possible to induce the regular oscillations where the slugs accumulate at the bottom of the cathode channel. But we have also observed the opposite effect where oscillations started about 8000 s after an increase in flows from $\xi = 1$ to $\xi = 1.3$ (the spatio-temporal data is available as Figure 4S in supplementary material available online).

The spatio-temporal current distribution in the vertical SAPC fuel cell with the gas flows upwards were complex and did not appear to be deterministic. At the same feed flow rates, load impedance, and temperature, the steady state settled into different spatio-temporal patterns including: (i) stable current with a constant current density profile along the length of the flow channel, (ii) oscillating currents with periods of 10–400 s that correlated with water slug motion along the channel, or (iii) irregularly fluctuating currents.

## Discussion

A number of studies have been published that have employed various visualization tools to examine water drops in PEM fuel cells, as referenced earlier. We also briefly discussed the very large number of studies that have modeled two-phase flow and liquid drops in PEM fuel cells. Our work presented here is one of the first to correlate flow visualization with local current density measurements. This work is also the first to directly observe the importance of orientation

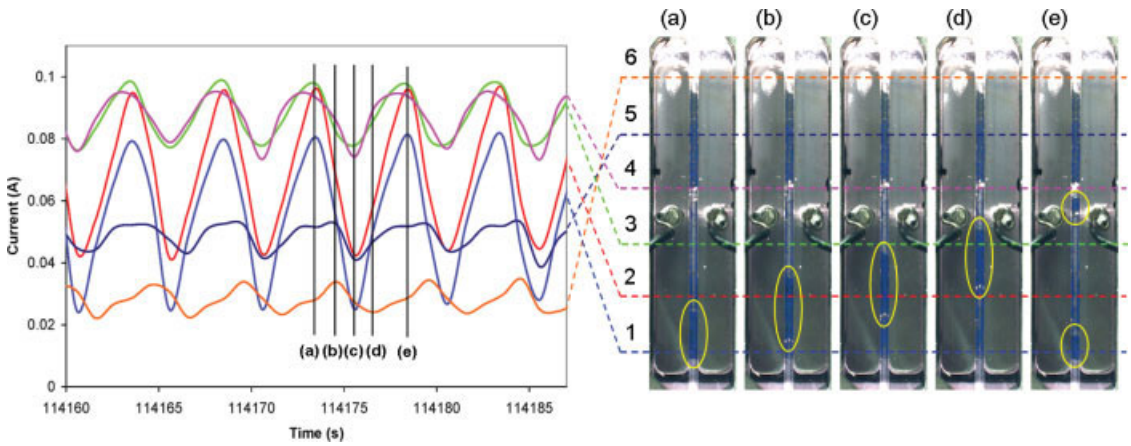


**Figure 16. Spatio-temporal correlation of local current and water slugs in the vertical SAPC fuel cell with the flows against gravity (V-ii).**

The current measurements are from the continuation of the data shown in Figure 15. Slugs form near the bottom of the MEA and are pushed part-way up the channel before falling back down to help create a new slug in the same location. [Color figure can be viewed in the online issue, which is available at www.interscience.wiley.com.]

and gravity on flooding in PEM fuel cells. Lastly, we provided clear visual evidence of liquid water flow through the GDL.

The results presented here suggest a significantly different physical basis for water transport in PEM fuel cells when compared with the common approaches found in the literature. A number of models have been proposed for water transport through the GDL. Most models employ Darcy's law to describe two phase flow in porous media,[1,3,5,6,39,40] as was done with some of the earliest published fuel cell models, such as that by Bernardi and Verbrugge.[41] Often, the models also include capillary condensation of water in the GDL.[1,2,4–6,40] Based on these assumptions, it is usually concluded that flooding causes all of the pores of the GDL to fill with water and any liquid that reaches the channel is either removed as mist in the gas streams or wicks onto the hydrophilic channel walls. Our data suggests a different interpretation of "flooding" in PEM fuel cells. Liquid water must be transported across the GDL due to a hydrostatic pressure gradient between the cathode catalyst/membrane interface and the cathode gas flow channel. A good GDL should be hydrophobic to inhibit capillary condensation of water. Liquid water only enters the largest pores in the GDL so that only a small number of pores are blocked to gas flow.

Once the water breaks through the GDL to the flow channel, our observations again suggest that different physical phenomena govern the motion of liquid water than those found in the PEMFC literature. Often, the surface tension between the liquid drops and the GDL surface is considered to be the most important force,[21] with gravity being neglected if mentioned at all. Assuming that the liquid drops are held to the GDL by the GDL/water surface tension, a few groups have examined how water droplets or films held to the GDL move along the channels and onto the channel walls. The interfacial energy of water with the GDL and the channel walls are the key system parameters for those models.[21,23,25] These numerical studies have also shown that hydrophilic channel walls are desirable, with the flow of water along the corners of the channel being an important mechanism for water removal. Other studies have focused on the deformation and movement of droplets attached to the GDL under different operating conditions.[1,18,25] It is thought that the surface tension forces are balanced by the drag force from the gas flow, while the droplet deforms until the it finally detaches. The important factors affecting how the droplets moved down the channel and interacted with the channel walls were found to be the gas flow, hydrophilicity/hydrophobicity of the channel walls, GDL surface, and temperature. In some cases it was concluded that the droplets that sat on top of the GDL blocked the flow of oxygen and could even form a film over the GDL. Our results suggest that drop detachment is the result of gravity or shearing forces overcoming the cohesive forces between the water in the GDL pore and the water drop on the surface of the GDL.

The results presented here paint a conceptually different physical picture of water transport and flooding than what has conventionally been assumed. We have shown that when placing the fuel cell with the cathode facing down there is no evidence of current reductions due to flooding even in the presence of liquid water in the gas flow channel. We conclude that no flooding occurs when gravity assists in keeping liquid water away from the GDL surface, indicating that flooding is not the result of capillary condensation in the GDL, but rather liquid blocking oxygen transport across the gas/GDL interface. We have also shown that drops are held in place due to the surface tension of water in the GDL pore, and gravity plays an important role in how the water drops detach. The experiments presented here lead to five important conclusions about how water is transported and is the cause of flooding in PEM fuel cells:

(1) The current reduction due to flooding in PEM fuel cells is the result of water slugs in the cathode flow channel.

(2) Liquid water is driven from the electrode/GDL interface to the gas flow channel by a hydraulic pressure through the largest pores in the GDL.

(3) Drops grow until gravity or the shearing force from gas flow overcomes surface tension and detaches the drop.

(4) The detached drops coalesce and grow into slugs in the cathode gas flow channel.

(5) Slug motion is critically dependent on the orientation of the flow channels.

Our data suggest it is impossible to give a complete description of the spatio-temporal current density in the simplest of two-dimensional fuel cells—a fuel cell with a single straight channel. We have shown very complex behavior that depends on two critical parameters: (i) the orientation of the fuel cell with respect to gravity, and (ii) the stoichiometry of the inlet feeds. Our simplified model fuel cell has helped us to isolate the key physics of water transport in a way previous investigators have not been able to. We will try to draw some general conclusions from the data presented here, but we admit this is only the beginning of identifying the essential physics that properly describe fuel cell operation.

### *Liquid water transport across in the gas diffusion layer*

Why must liquid water be transported hydraulically across the GDL? As illustrated in Figure 2, water is formed at the membrane/cathode interface and must make its way to the cathode gas flow channel to be removed. If there is any liquid water in the gas flow channel, the water activity is unity both at the membrane/electrode interface and in the cathode gas flow channel. With equal water activity, there is no driving force for diffusion across the GDL. As we have shown, along with virtually every other investigator, PEM fuel cells operate with liquid water present in the gas flow channel, hence there must be a mechanism to move liquid water across the GDL. The only way to move a liquid through a porous medium is to apply a hydraulic pressure.

Why must the GDL be hydrophobic? If the GDL were hydrophilic, water would be wicked by capillary action into the GDL. Since there is liquid water in the gas flow channel there would be no driving force for liquid to move from the pores of the GDL into the gas flow channel. The pores of the GDL would become saturated with liquid with no way to escape. This would block any gas transport from the gas flow channel through the GDL to the membrane/electrode interface. The only way to permit gas transport across the GDL in the presence of liquid water is for the GDL to be hydrophobic.

Because the GDL is hydrophobic it expels liquid water. To get liquid water to pass through the GDL, the liquid must be pushed by a hydraulic pressure sufficient to overcome the surface energy of the water/GDL interface. The results summarized in Table 1 and illustrated in Figure 5 show that no liquid water will flow through the GDL until the hydrostatic pressure is raised to a level that overcomes the surface energy in the pores of the GDL. The force required to penetrate the pore scales inversely with the pore radius, $r_{\text{pore}}$, so the liquid water will first penetrate the largest pores. The critical pore size for liquid penetration is given by Eq. 1, where $\gamma_{\text{GDL/water}} = \gamma_{\text{water}}\cos\theta$ is the interfacial energy for the GDL/water interface and $\theta$ is the contact angle.

$$\Delta P = \frac{2\gamma_{\text{GDL/water}}}{r_{\text{pore}}} \tag{1}$$

Most GDL media are treated with Teflon to make them more hydrophobic. The contact angle between water and Teflon is reported to be 112°.[42] Based on the Teflon/water contact angle and the critical hydrostatic pressure to initiate water flow through the GDL media, we can determine the pore radius where the water first penetrates.

Once liquid penetrates the pores, it freely flows through. As a first approximation, the flow through the pore is described by Poiseuille flow. The flow rate through a single pore, $Q_{\text{pore}}$, is proportional to the hydrostatic pressure, as given by Eq. 2.

$$Q_{\text{pore}} = \frac{\pi r_{\text{pore}}^4 \Delta P}{8\mu_{\text{water}} L_{\text{pore}}} \tag{2}$$

Once a pore is breached, water flow will continue until all the liquid is drained through the pore even though the hydrostatic pressure has dropped below the critical pressure. This is because once the pore is filled with liquid there is no longer a resistance to liquid water entering the pore. If the applied hydrostatic pressure is greater than the minimum required to start flow through the largest pore, liquid can breach slightly smaller pores and the total liquid flow is increased.

### *Water drop detachment*

As the water flows through the GDL, it forms a drop at the surface. Since the GDL surface is hydrophobic, there is no cohesive force holding a drop to the GDL surface. In the experimental data reported here, the drops must be held in place by the cohesive force between the water in the drop and the water in pore. The drops grow until the force of gravity on the drop exceeds the surface tension holding the drop in place; the force balance for the critical drop size for detachment is given by Eq. 3.

$$2\pi\gamma_{\text{water}} r_{\text{pore}} = \frac{4}{3}\pi r_{\text{drop}}^3 \rho_{\text{water}} g \tag{3}$$

The hydrostatic pressure to force water through the pores increases inversely with the pore radius. There are pores in the carbon cloth that are larger than the pores in the carbon paper, and therefore less hydrostatic pressure head is required to push liquid water through the carbon cloth. The pressures required to push water through the pores are quite modest (1–10 kPa). A higher pressure is required to force liquid through the pores of the carbon paper, but the drops that form are smaller when they detach, and the smaller pores permit less liquid flow. The data presented in Table 1 show excellent agreement with Eq. 3. The critical pore radius for liquid to breach the GDL decreased by a factor of 7 from cloth to paper. Equation 3 suggests the critical drop size for detachment should decrease by $\sqrt[3]{7} = 1.9$ between the two GDL materials, which is close to the experimental value of 2.1.

The photographic sequence in Figure 5 shows that only a single pore permitted liquid flow at the critical hydrostatic pressure head over an area of 5 $cm^2$. The total flow rate through that single pore was ~1.5 mL/min for carbon cloth and ~0.25 mL/min for carbon paper. At a fuel cell current density of 1 $A/cm^2$, the required liquid flow rate to drain the water away would be 0.011 $mL/(min \cdot cm^2)$, so that only a single pore is needed to carry all the liquid water from more than 10 $cm^2$. Since liquid only breaches the largest pores and only a single 25-$\mu$m pore is required to carry the liquid product from 1 $cm^2$ of the MEA, almost all the GDL pores remain free of liquid and permit gas to diffuse to the membrane/electrode interface.

The water at the membrane/electrode interface accumulates as it forms. Since it is in a confined space, the accumulating water will build up the hydrostatic pressure necessary to push the liquid through the largest pores. The pores in the GDL are interconnected within the plane and so the liquid water will search for the path of least resistance to push through to the gas flow channel. Other investigators who have seen droplets on the surface of the GDL ascribe the resistance to motion as resulting from the interfacial energy between the GDL and the droplet. Our results suggest that water drops move along the hydrophobic GDL surface with little force from the gas flow. It is the surface tension between the drop and the water in the GDL pore that holds the drops in place and must be overcome.

### *Mechanism of cathode flooding*

If liquid water does not flood the pores of the GDL what is the mechanism of flooding in PEM fuel cells? Our results from the SAPC fuel cell in different orientations shows that the current in the fuel cell only drops when liquid water accumulates in the cathode gas flow channel in a way that inhibits oxygen transport into the GDL. When the flow channel is horizontal with the cathode facing downward and when the flow channel is vertical with the gas flow going in the direction of gravity, there was no evidence of any current reduction from flooding by liquid water unless the oxygen feed was totally consumed by reaction. In both of these configurations liquid water drainage is assisted by gravity.

When the gas flow rate to the cathode was reduced so that the oxygen feed was totally consumed there was only gravity to assist in the liquid water removal. This resulted in the "periodic" spikes in the current shown in Figure 8 for $\xi_1$. The water would build up near the outlet of the flow channel. This caused a reduction in current in electrode segment 6, resulting in a slight excess of oxygen in the feed. The oxygen pressure would build up until it pushed a water slug out

of the gas outlet of the fuel cell. The same phenomenon was observed with the fuel cell oriented vertically with the gas flows going downward. It might have been expected that the water would drain from the fuel cell just by gravity. However, the stainless steel electrodes along the sides of the flow channel are slightly hydrophilic and hold drops in place near the bottom of the flow channel in the absence of any gas flow. This gives rise to similar behavior as that seen in Figure 8.

Placing the SAPC fuel cell horizontal with the cathode facing up or placing the fuel cell vertical with the cathode flow going upwards, counter to gravity, both create situations where gravity plays a much greater role in the flooding. With the horizontal orientation, the water drops form on the GDL but it is only the shearing force from the gas flow that can detach the drops and force them to move. If the drops are sufficiently small so they do not significantly disrupt the gas flow field, the critical drop size can be found by balancing the shear force from the gas multiplied by the area of the drop with the surface energy holding the drop to the pore in the GDL.

$$\left(\frac{4\mu_{\text{gas}}Q_{\text{gas}}}{\pi r_{\text{channel}}^3}\right)\left(\pi r_{\text{drop}}^2\right) > 2\pi r_{\text{pore}}\gamma_{\text{water}} \tag{4}$$

A critical drop size for detachment can be identified from the force balance. At the flow rates in the SAPC fuel cell ($Q$ = 0.1 cm$^3$/s, $v$ = 100 cm/s) the critical drop size is 2 cm, which is larger than the flow channel. This implies that simple shearing action is not sufficient for the drop detachment. Rather what must happen is the drop will grow until it spans the gas flow channel and blocks the gas flow. The gas pressure will increase until it is sufficient to detach the drop; the required pressure for drop detachment is given by Eq. 5.

$$\Delta P = \frac{\rho_{\text{gas}}Q_{\text{gas}}^2}{2\pi^2 r_{\text{channel}}^4} > \frac{2r_{\text{pore}}\gamma_{\text{water}}}{r_{\text{channel}}^2} \tag{5}$$

In the SAPC fuel cell ($r_{\text{channel}}$ = 1 mm), the required pressure to detach the drops that span the channel is 10 Pa. In large fuel cells where the gas flow rates and velocities in the small channels are much larger, the shearing force of the gas can become sufficient to detach liquid drops from the GDL. For a 1000 cm$^2$ $H_2/O_2$ fuel cell operating at 0.5 A/cm$^2$ with $\xi_2$, the cathode flow rate is 50 cm$^3$/s, $v$ = 50,000 cm/s, and the critical radius for drop detachment is 0.3 mm. However, when the cell size decreases to 100 cm$^2$, the gas velocities are no longer sufficient to cause drop detachment by shearing action and water drops that span the flow channels will be observed.

After drops detach from the anchoring pore, they require little force to move and so they are pushed to the end of the cathode gas flow channel. In the SAPC fuel cell, the flow channel turns 90° to exit. In the horizontal configuration with the cathode facing up, H-ii, the exit flow points up against gravity. Because of the configuration of the fuel cell and exit tube, liquid water forms drops that, after detachment, are pushed toward the outlet of the flow channel. The drops are held up until the pressure is sufficient to push the water up against gravity into the exit tube. The drops tend to accumulate at the exit end of the flow channel and coalesce to form larger drops and slugs. The data in Figure 9 shows that the slugs grow and inhibit oxygen transport to the membrane/electrode interface near the outlet of the flow channel. The slug growth blocks the gas flow so a pressure builds up and eventually pushes the slug out of the channel. The slug growth and push out is evident in Figure 9 where the currents fluctuate the most in electrode segments 4, 5, and 6, but the currents are almost constant in the upstream electrode segments.

The effect of gravity is most dramatic for the SAPC fuel cell vertically oriented with the cathode flow rising upwards against gravity. As shown earlier, the gas flow rate is insufficient to cause the drops to detach as they grow at the surface of the GDL, so drops instead will fall due to gravity. The most commonly observed behavior is that the drops fall to the bottom of the cathode gas flow channel, where they coalesce to form slugs. When the slugs first form, they are sufficiently small and the gas can deform them and flow past. As the slugs get larger, the pressure drop associated with slug deformation becomes too great and the slugs span the channel, blocking gas from moving up the channel. The gas pressure builds up and pushes the slug up the column. The gas pressure must overcome the gravitational force associated with the slug, as given by Eq. 6.

$$\Delta P = \frac{\rho_{\text{gas}}Q_{\text{gas}}^2}{2\pi^2 r_{\text{channel}}^4} > L_{\text{slug}}\rho_{\text{water}}g \tag{6}$$

At the top of the cathode gas flow channel, the flow encounters a 90° angle. The slugs break apart at the top so that a smaller slug of water is pushed out of the exit tube, and the rest of the water flows back down the channel and is incorporated into forming a new liquid slug.

### *Slug formation and motion*

The details of the process of slug formation, motion, and the gas flow are hard to predict quantitatively, but certain trends are evident. At sufficiently high gas flow rates, the slugs are continually formed and pushed up the channel with little or no change in the currents from the six electrode segments. This appears to correspond to the slugs moving up the channel over a short period of time, where the liquid does not remain in any position long enough to hinder oxygen transport to the membrane/electrode interface. Reducing the oxygen flow rate where there is little stoichiometric excess results in the slugs temporarily blocking the oxygen flow and causing large current fluctuations. Figure 16 shows that just after the slug forms and blocks the gas flow, the currents start to drop in all the electrode segments. The local current turns on as the slug moves up the channel. The currents continue to rise until the next slug has grown sufficiently large to block the flow channel and the process repeats itself.

The process of slug formation and rising in the vertical cathode flow channel occurs over a period of 10–30 s. The typical slug as shown in Figure 16 is 0.025 cm$^3$. The rate of water formation in Figure 15 is 5–10 cm$^3$/s, so it should take 2500 s to form a slug from just the water produced by reaction. Slug formation is much faster. This is clear evidence of slug breakup within the flow channel as 90% of the water in

the slug must rain back down the flow channel to form a new slug. Slug formation and breakup is common in gas–solid fluidized beds, which seems most analogous to the liquid water motion in the vertical SAPC fuel cell.

Many complex water distributions were observed that gave rise to highly variable dynamic current distribution patterns. For example, stopping the reactant flows to the horizontal SAPC fuel cell with the cathode facing up for several minutes resulted in a water film spreading across the entire GDL. When the reactant feeds were restarted, the currents in all electrode segments were reduced by more than an order of magnitude and it took several hours before fuel cell operation returned to its pre-shutdown performance.

The complexity of behavior is partially captured in Figures 8, 9, 12, and 15. Our intentions here are to illustrate the basic physics that affect water transport and flooding in PEM fuel cells; models that can capture all the complexities are far from being realized. Detachment of drops and movement of slugs is a function of gas flow rate; drops will coalesce as they move along the flow channel and will grow and make slugs. Smaller drops and slugs move faster than larger ones so that the small ones will overtake the larger ones and combine to make even larger slugs. Additionally, the gas velocity decreases from the inlet to the outlet, depending on the current, as per Eq. 7.

$$Q_{\text{gas}}(x) = Q_{\text{gas}}^{\text{inlet}}\left(1 - \frac{w_{\text{channel}}}{4\text{F}}\int_{\text{inlet}}^{x} J(x)dx\right) \tag{7}$$

The decrease in the gas velocity along the length of the cathode gas flow channel will result in slugs slowing down as they approach the outlet and grow to block the gas from getting to the membrane/electrode interface. This is what we reported for the SAPC fuel cell in the horizontal configuration with the cathode facing up. The water slugs build up at the end of the flow channel and cause a current drop in the electrode segments near the outlet.

A secondary effect of the inlet flow rates observed in the SAPC fuel cell was the redistribution of the current. Reducing the inlet gas flow rates caused the current density to increase at the upstream electrode segments and decrease at the downstream electrode segments. The decrease at the downstream segments was anticipated because the depletion of the reactants would reduce the chemical potential driving force for the current. However, the increase in the current density at the upstream electrode segments was unexpected. We propose that the current redistribution is due to lateral currents that result from the changes in the potential distribution associated with the depletion of the reactants.[36–38] When the reactant flows were reduced to partially starve the fuel cell, the upstream electrode segments are at higher potential differences than the down stream electrode segments. This causes the currents to be concentrated in the upstream electrode segments. We are presently building a fuel cell with a segmented anode and cathode to more effectively probe the current redistribution.

### *Implications for fuel cell design and operation*

The results presented here indicate some deficiencies in understanding the physics of liquid motion in PEM fuel cells. Yet, with our results, we can start to think about how to improve the designs of fuel cell systems and materials. One consideration is with the GDL. The best GDL material will have a bimodal pore distribution—large pores to carry water from the membrane/electrode interface into the gas flow channel and small pores to carry oxygen from the gas flow channel to the membrane/electrode interface. Liquid drops form on the surface of the GDL as water emerges from the largest pores. The flow channels should be designed so that slug and drop motion to remove the liquid water can be facilitated by gas flow or gravity.

In practice, there are a variety of approaches that have been proposed to deal with flooding in PEM fuel cells. The most common approach is to employ excess reactant flows so the gas velocities are sufficiently high to blow liquid water out of the flow channels. A variety of flow channel configurations are available commercially and others are reported in the literature; most being variations on serpentine flow channels.[43–47] It appears that the required flow rates to remove liquid water have been determined through operational experience—we have not seen any models for multiphase flow that predict the required flow rates. Other approaches to manage liquid water include porous electrodes to wick liquid water from the cathode flow channel, and controlled temperature gradients along the flow channels to increase water vapor flow.[48,49]

The standard fuel cell design employing serpentine flow channels may be best for fuel cells operating in the "zero-G" environments of space vehicles,[50] but they may not be a good design for operation on earth. The results presented here point out that the orientation of the flow fields with respect to gravity plays an important role in fuel cell flooding. Our group introduced the self-draining channel-less PEM fuel cell that could operate with Nafion membranes utilizing dry feeds.[51] By removing the flow channels we could permit liquid water exiting the GDL to drain by gravity. We found no evidence of flooding in the self-draining fuel cell to current densities $> 2$ A/cm$^2$ at temperatures of 25–80°C with $H_2/O_2$ feeds at exact stoichiometry of hydrogen and stoichiometric excess of 30% oxygen.[35] Recently Honda introduced gravity-assisted draining in their new parallel flow channel fuel cell design,[52] but there are no details of its operating characteristics.

Besides channel orientation, the gas flow rate also plays an important role in the motion of liquid drops and slugs in flow channels of fuel cells. This has important implications in control of the cathode feed rate for load following. As the power output (or current output) is reduced, the feed rate is generally reduced in direct proportion to the current. This keeps the volume fraction of liquid drops and slugs constant. However, as shown earlier, the speed of the detachment of drops and motion of the slugs depends on the gas flow rate or gas flow rate squared; so reducing the gas flow rate with reduced current can result in more coalescence of drops and slugs leading to current fluctuations. Flow control for load following must take into account the problem of slug motion in the flow channels. We should point out that flooding and cathode inlet feed control is less of a problem with air than with oxygen. The large amount of nitrogen associated with air causes a large increase in the gas flow rate, and much less decrease in the flow rate along the length of the flow

channel, both of which improve the removal of liquid slugs. On the negative side, the higher flow rate of the air also acts to dry the membrane, which may require greater humidification of the cathode feed. The implications are that the optimal fuel cell flow system design and control may be different for the $H_2/O_2$ and $H_2$/air fuel cells, and the design should make that distinction.

## Conclusions

Experiments have been presented that illuminate the physics of liquid water transport in PEM fuel cells. The key experimental results are as follows:

(1) Water accumulates at the membrane/electrode interface until sufficient hydrostatic pressure builds up to overcome the water/GDL interfacial tension.

(2) Liquid water enters the largest pores of the GDL and flows from the membrane/electrode interface to the cathode gas flow channel.

(3) Water drops form on the surface of the GDL, which are held in place by cohesive forces with water in the pores. The drops detach when gravity or shear forces overcome the cohesive forces.

(4) Most of the pores of the GDL remain free of any liquid due to their hydrophobicity.

(5) After a water drops detaches, it moves freely along the surfaces in the gas flow channel, running into other drops and combining to form liquid slugs.

(6) Liquid slugs grow until they hinder the gas flow in the cathode flow channel.

(7) Flooding occurs when liquid water slugs hinder the gas transport downstream and cause the starvation of the reactants to the membrane/electrode interface.

(8) The motion of liquid slugs is gravity dependent.

(a) If the fuel cell is oriented such that gravity assists the removal of liquid from the cathode gas flow channel, the fuel cell will operate stably.

(b) When the fuel cell is oriented such that the gas flow must push the liquid slugs against gravity, reactant gas flow is temporarily blocked, resulting in large current density fluctuations.

Our results suggest that new models for PEM fuel cells are needed. Standard computational fluid dynamic models that are being pursued extensively for PEM fuel cell design are not adequate to capture the physics associated with flooding. The water transport pores in the GDL are randomly distributed and the gas flow decreases along the length of the gas flow channels due to reaction. CFD models are not able to deal with two phase flow systems where the relative fraction of the two phases is changing as a function of time and position. It is more likely that probabilistic models can more successfully capture the complexity associated with multiphase flow in PEM fuel cells.

Note: Extra figures are available online as supplementary material, as mentioned earlier. Briefly, they include a photo of the GDL permeation experiment setup (Figure 1S), a photo of the SAPC fuel cell system setup (Figure 2S), a graph of spatio-temporal data for configuration V-ii showing step-wise flow decreases (Figure 3S), and a graph of spatio-temporal data for configuration V-ii showing a response to a flow increase (Figure 4S).


## Acknowledgments

We thank the National Science Foundation (CTS -0354279) for support of this work. E. Kimball also thanks the Princeton University Program in Plasma Science and Technology for partial support under U.S. Department of Energy, Contract No. DE-AC02-76-CHO-3073.


## Notation

H-i = configuration with flow channels horizontal and the cathode facing down
H-ii = configuration with the flow channels horizontal and the cathode facing up
V-i = configuration with the flow channels vertical and the inlets at the top
V-ii = configuration with the flow channels vertical and the inlets at the bottom
$F_{H2}$ = flow rate of hydrogen in the anode side flow channel, $cm^3/min$
$F_{O2}$ = flow rate of oxygen in the cathode side flow channel, $cm^3/min$
r = radius, cm
$P$ = pressure, Pa
$Q$ = volumetric flow rate, $cm^3/min$
$L$ = length, cm
g = acceleration of gravity, $cm/s^2$
$v$ = linear velocity, cm/s
$w$ = width, cm
F = Faraday's constant, 96458.3 C/(mol $e^-$)
$J$ = current density, $A/cm^2$

### *Greek letters*

$\xi$ = stoichiometry; the ratio of gas supplied in the feed to gas consumed by the electrochemical reaction
$\gamma$ = surface tension, dyne/cm
$\theta$ = contact angle
$\mu$ = viscosity, Pa·s
$\rho$ = density, $g/cm^3$

### *Subscripts*

pore = pore of the gas diffusion layer
GDL/water = interface between the GDL and the water in a pore
water = water in the pores and/or flow channels
gas = gas in the flow channel (oxygen on the cathode side; hydrogen on the anode side)
channel = flow channel
drop = drop forming at the surface of the GDL
slug = slug of water completely blocking the flow channel on the cathode side

### *Superscripts*

inlet = at the inlet to the flow channel

## Literature Cited


1. He GL, Ming PW, Zhao ZC, Abudula A, Xiao Y. A two-fluid model for two-phase flow in PEMFCs. *J Power Sources*. 2007;163:864–873.
2. Liu ZX, Mao ZQ, Wang C. A two dimensional partial flooding model for PEMFC. *J Power Sources*. 2006;158:1229–1239.
3. Meng H, Wang CY. Model of two-phase flow and flooding dynamics in polymer electrolyte fuel cells. *J Electrochem Soc*. 2005;152: A1733–A1741.
4. Natarajan D, Van Nguyen T. Three-dimensional effects of liquid water flooding in the cathode of a PEM fuel cell. *J Power Sources*. 2003;115:66–80.

5. Wang ZH, Wang CY, Chen KS. Two-phase flow and transport in the air cathode of proton exchange membrane fuel cells. *J Power Sources*. 2001;94:40–50.
6. Weber AZ, Darling RM, Newman J. Modeling two-phase behavior in PEFCs. *J Electrochem Soc*. 2004;151:A1715–A1727.
7. Benziger J, Nehlsen J, Blackwell D, Brennan T, Itescu J. Water flow in the gas diffusion layer of PEM fuel cells. *J Membr Sci*. 2005;261:98–106.
8. Litster S, Sinton D, Djilali N. Ex situ visualization of liquid water transport in PEM fuel cell gas diffusion layers. *J Power Sources*. 2006;154:95–105.
9. Fairweather JD, Cheung P, St-Pierre J, Schwartz DT. A microfluidic approach for measuring capillary pressure in PEMFC gas diffusion layers. *Electrochem Comm*. 2007;9:2340–2345.
10. Gostick JT, Fowler MW, Ioannidis MA, Pritzker MD, Volfkovich YM, Sakars A. Capillary pressure and hydrophilic porosity in gas diffusion layers for polymer electrolyte fuel cells. *J Power Sources*. 2006;156:375–387.
11. Hickner MA, Siegel NP, Chen KS, McBrayer DN, Hussey DS, Jacobson DL, Arif M. Real-time imaging of liquid water in an operating proton exchange membrane fuel cell. *J Electrochem Soc*. 2006;153:A902–A908.
12. Owejan JP, Trabold TA, Jacobson DL, Baker DR, Hussey DS, Arif M. In situ investigation of water transport in an operating PEM fuel cell using neutron radiography, Part 2: Transient water accumulation in an interdigitated cathode flow field. *Int J Heat Mass Transfer*. 2006;49:4721–4731.
13. Pekula N, Heller K, Chuang PA, Turhan A, Mench MM, Brenizer JS, Unlu K. Study of water distribution and transport in a polymer electrolyte fuel cell using neutron imaging. *Nucl Instrum Methods Phys Res Section A: Accelerators Spectrometers Detectors Associated Equipment*. 2005;542:134–141.
14. Trabold TA, Owejan JP, Jacobson DL, Arif M, Huffman PR. In situ investigation of water transport in an operating PEM fuel cell using neutron radiography, Part 1: Experimental method and serpentine flow field results. *Int J Heat Mass Transfer*. 2006;49:4712–4720.
15. Turhan A, Heller K, Brenizer JS, Mench MM. Quantification of liquid water accumulation and distribution in a polymer electrolyte fuel cell using neutron imaging. *J Power Sources*. 2006;160:1195–1203.
16. Liu X, Guo H, Ma CF. Water flooding and two-phase flow in cathode channels of proton exchange membrane fuel cells. *J Power Sources*. 2006;156:267–280.
17. Ma HP, Zhang HM, Hu J, Cai YH, Yi BL. Diagnostic tool to detect liquid water removal in the cathode channels of proton exchange membrane fuel cells. *J Power Sources*. 2006;162:469–473.
18. Theodorakakos A, Ous T, Gavaises A, Nouri JM, Nikolopoulos N, Yanagihara H. Dynamics of water droplets detached from porous surfaces of relevance to PEM fuel cells. *J Colloid Interface Sci*. 2006;300:673–687.
19. Tuber K, Pocza D, Hebling C. Visualization of water buildup in the cathode of a transparent PEM fuel cell. *J Power Sources*. 2003;124:403–414.
20. Yang XG, Zhang FY, Lubawy AL, Wang CY. Visualization of liquid water transport in a PEFC. *Electrochem Solid State Lett*. 2004; 7:A408–A411.
21. Zhang FY, Yang XG, Wang CY. Liquid water removal from a polymer electrolyte fuel cell. *J Electrochem Soc*. 2006;153:A225–A232.
22. Jiao K, Zhou B, Quan P. Liquid water transport in straight microparallel-channels with manifolds for PEM fuel cell cathode. *J Power Sources*. 2006;157:226–243.
23. Quan P, Lai MC. Numerical study of water management in the air flow channel of a PEM fuel cell cathode. *J Power Sources*. 2007;164: 222–237.
24. Cai YH, Hu J, Ma HP, Yi BL, Zhang HM. Effects of hydrophilic/hydrophobic properties on the water behavior in the micro-channels of a proton exchange membrane fuel cell. *J Power Sources*. 2006; 161:843–848.
25. Zhan ZG, Xiao JS, Pan M, Yuan RZ. Characteristics of droplet and film water motion in the flow channels of polymer electrolyte membrane fuel cells. *J Power Sources*. 2006;160:1–9.
26. Araki T, Koori H, Taniuchi T, Onda K. Simulation of the current density distribution for a PEMFC by using measured electrochemical and physical properties of the membrane. *J Power Sources*. 2005; 152:60–66.
27. Buchi FN, Geiger AB, Neto RP. Dependence of current distribution on water management in PEFC of technical size. *J Power Sources*. 2005;145:62–67.
28. Hakenjos A, Hebling C. Spatially resolved measurement of PEM fuel cells. *J Power Sources*. 2005;145:307–311.
29. Natarajan D, Van Nguyen T. Current distribution in PEM fuel cells, Part 1: Oxygen and fuel flow rate effects. *AIChE J*. 2005;51:2587–2598.
30. Nishikawa H, Kurihara R, Sukemori S, Sugawara T, Kobayashi H, Abe S, Aoki T, Ogami Y, Mutsunaga A. Measurements of humidity and current distribution in a PEFC. *J Power Sources*. 2006;155:213–218.
31. Benziger JB, Chia ES, De Decker Y, Kevrekidis IG. Ignition and front propagation in polymer electrolyte membrane fuel cells. *J Phys Chem C*. 2007;111:2330–2334.
32. Patterson TW, Darling RM. Damage to the cathode catalyst of a PEM fuel cell caused by localized fuel starvation. *Electrochem Solid State Lett*. 2006;9:A183–A185.
33. Reiser CA, Bregoli L, Patterson TW, Yi JS, Yang JDL, Perry ML, Jarvi TD. A reverse-current decay mechanism for fuel cells. *Electrochem Solid State Lett*. 2005;8: A273–A276.
34. Taniguchi A, Akita T, Yasuda K, Miyazaki Y. Analysis of electrocatalyst degradation in PEMFC caused by cell reversal during fuel starvation. *J Power Sources*. 2004;130:42–49.
35. Woo CH, Benziger JB. PEM fuel cell current regulation by fuel feed control. *Chem Eng Sci*. 2007;62:957–968.
36. Kulikovsky AA. Voltage loss in bipolar plates in a fuel cell stack. *J Power Sources*. 2006;160:431–435.
37. Santis M, Freunberger SA, Papra M, Wokaun A, Buchi FN. Experimental investigation of coupling phenomena in polymer electrolyte fuel cell stacks. *J Power Sources*. 2006;161:1076–1083.
38. Berg P, Promislow K, Stumper J, Wetton B. Discharge of a segmented polymer electrolyte membrane fuel cell. *J Fuel Cell Sci Tech*. 2005;2:111–120.
39. Lin GY, He WS, Van Nguyen T. Modeling liquid water effects in the gas diffusion and catalyst layers of the cathode of a PEM fuel cell. *J Electrochem Soc*. 2004;151:A1999–A2006.
40. Pasaogullari U, Wang CY. Liquid water transport in gas diffusion layer of polymer electrolyte fuel cells. *J Electrochem Soc*. 2004;151: A399–A406.
41. Bernardi DM, Verbrugge MW. A mathematical-model of the solid-polymer-electrolyte fuel-cell. *J Electrochem Soc*. 1992;139:2477–2491.
42. Adamson AW. *Physical Chemistry of Surfaces*, 5th ed. NY: Wiley, 1990.
43. Xu C, Zhao TS. A new flow field design for polymer electrolyte-based fuel cells. *Electrochem Commun*. 2007;9:497–503.
44. Kitta S, Okumoto T, Uchida H, Watanabe M. New metal separators coated with carbon/resin composite layers for PEFCs. *Electrochemistry*. 2007;75:213–216.
45. Kumar A, Reddy RG. Effect of gas flow-field design in the bipolar/end plates on the steady and transient state performance of polymer electrolyte membrane fuel cells. *J Power Sources*. 2006;155:264–271.
46. Nikam VV, Reddy RG. Corrugated bipolar sheets as fuel distributors in PEMFC. *Int J Hydrogen Energy*. 2006;31:1863–1873.
47. Yan WM, Yang CH, Soong CY, Chen FL, Mei SC. Experimental studies on optimal operating conditions for different flow field designs of PEM fuel cells. *J Power Sources*. 2006;160:284–292.
48. Dufner BF, Perry ML, Trocciola JC, Yang D, Yi JS; UTC Fuel Cells, LLC, assignee. Bi-zone water transport plate for a fuel cell. US Patent 6,617,068, September 9 (2003).
49. Voss HH, Wilkinson DP, Watkins DS; Ballard Power Systems Inc., assignee. Method and apparatus for removing water from electrochemical fuel cells by controlling the temperature and pressure of the reactant streams. US Patent 5,441,819, August 15 (1995).
50. Sone Y, Ueno M, Naito H, Kuwajima S. One kilowatt-class fuel cell system for the aerospace applications in a micro-gravitational and closed environment. *J Power Sources*. 2006;157:886–892.
51. Hogarth WHJ, Benziger JB. Operation of polymer electrolyte membrane fuel cells with dry feeds: design and operating strategies. *J Power Sources*. 2006;159:968–978.
52. Komura T, Moriya T, Isobe S, Ushiro T; Honda Giken Kogyo Kabushiki Kaisha, assignee. Fuel cell system and draining method for the same. US Patent 6,242,119, June 5, 2001.

*Manuscript received July 20, 2007, and revision received Jan. 8, 2008.*

## Appendix. Summary of Data Files

| Flow Config-uration | Flow Direc-tion | QH2 | QO2 | i1 | i2 | i3 | i4 | i5 | i6 | V | itot | Stability | Duration | Period of oscillations | Max. (by seg.) magnitude of fluctuations | Phase change | File name |
|---|---|---|---|---|---|---|---|---|---|---|---|---|---|---|---|---|---|
| h-i | cnt | 12 | 12 | 0.0808 | 0.1137 | 0.1485 | 0.1858 | 0.1544 | 0.1448 | 0.4710 | 0.828 | Steady | 9000 s | n/a | n/a | n/a | MEA5-25-constcnt-flooding-cathodedown |
| h-i | cnt | 6 | 3 | 0.0966 | 0.1351 | 0.1659 | 0.1718 | 0.1078 | 0.0794 | 0.4274 | 0.757 | Irregular fluctuations | 66,000 s | 2100 s | Max of 40% at 6 | Between 4 & 5 | MEA5-25-constcnt-flooding-cathodedown |
| h-i | cnt | 12 | 12 | 0.0857 | 0.1009 | 0.1394 | 0.1946 | 0.1745 | 0.1671 | 0.4924 | 0.862 | Steady | 10,800 s | n/a | n/a | n/a | MEA5-25-constcnt-flooding-cathodedown |
| h-i | cnt | 6 | 3 | 0.0891 | 0.1210 | 0.1478 | 0.1389 | 0.1295 | 0.1164 | 0.4190 | 0.743 | Irregular fluctuations | 8000 s | 2100 s | Max of 30% at 6 | At 4 | MEA5-25-constcnt-flooding-cathodedown2 |
| h-i | cnt | 12 | 6 | 0.0822 | 0.1128 | 0.1448 | 0.1465 | 0.1553 | 0.1585 | 0.4547 | 0.8 | Steady | 81,000 s | n/a | n/a | n/a | MEA5-25-constcnt-flooding-cathodedown2 |
| h-i | cnt | 6 | 3 | 0.0964 | 0.1272 | 0.1646 | 0.1421 | 0.1184 | 0.0931 | 0.4183 | 0.742 | Irregular fluctuations | 20,000 s | 1600 s | Max of 40% at 6 | At 4 | MEA5-25-constcnt-flooding-cathodedown2 |
| h-i | co | 6 | 3 | 0.1464 | 0.1786 | 0.1583 | 0.1599 | 0.0899 | 0.0614 | 0.4461 | 0.794 | Irregular spiked fluctuations | 5000 s | 1500 s | Max of 50% at 6 | Between 3 & 4 | MEA5-25-constco-flooding-cathodedown |
| h-i | co | 7 | 3.5 | 0.1180 | 0.1506 | 0.1477 | 0.1778 | 0.1406 | 0.1614 | 0.5080 | 0.896 | Oscillations died out | 7000 s | n/a | n/a | n/a | MEA5-25-constco-flooding-cathodedown |
| h-i | co | 8 | 4 | 0.1237 | 0.1513 | 0.1462 | 0.1803 | 0.1465 | 0.1728 | 0.5247 | 0.921 | Steady | 67,000 s | n/a | n/a | n/a | MEA5-25-constco-flooding-cathodedown |
| h-ii | cnt | 12 | 12 | 0.1215 | 0.0893 | 0.1336 | 0.1851 | 0.1670 | 0.1645 | 0.4922 | 0.861 | Steady | 6000 s | n/a | n/a | n/a | MEA5-25-constcnt-flooding-anodedown |
| h-ii | cnt | 12 | 12 | 0.1955 | 0.1376 | 0.1245 | 0.0698 | 0.0294 | 0.0170 | 0.3163 | 0.574 | Redistribution (no system change) then steady | 5000 s | n/a | n/a | Between 3 & 4 | MEA5-25-constcnt-flooding-anodedown |
| h-ii | cnt | 12 | 12 | 0.1831 | 0.1535 | 0.1284 | 0.0695 | 0.0302 | 0.0173 | 0.3219 | 0.581 | Steady except for large redistribution after ~6600 s | 21,000 s | n/a | n/a | At 3 | MEA5-25-constcnt-flooding-anodedown2 |
| h-ii | cnt | 6 | 6 | 0.1862 | 0.1360 | 0.0973 | 0.0530 | 0.0240 | 0.0144 | 0.2774 | 0.511 | Slowly decreasing | 2500 s | n/a | n/a | n/a | MEA5-25-constcnt-flooding-anodedown2 |
| h-ii | cnt | 6 | 3 | 0.1845 | 0.1490 | 0.1211 | 0.0641 | 0.0279 | 0.0167 | 0.3085 | 0.563 | Large spike then steady | 3000 s | ~1000 s (single spike) | 200% on 3 (single spike) | At 2 | MEA5-25-constcnt-flooding-anodedown2 |
| h-ii | co | 6 | 3 | 0.1615 | 0.2014 | 0.1787 | 0.1306 | 0.0639 | 0.0401 | 0.4343 | 0.776 | Steady | 2000 s | n/a | n/a | n/a | MEA5-25-constco-flooding-cathodeup |
| h-ii | co | 12 | 6 | 0.1212 | 0.1629 | 0.1714 | 0.1762 | 0.1404 | 0.1314 | 0.5117 | 0.903 | Oscillations in segment 6 | 8000 s | 750 s | 10% at 6 | n/a | MEA5-25-constco-flooding-cathodeup |
| h-ii | co | 6 | 3 | 0.1652 | 0.2054 | 0.1802 | 0.1287 | 0.0622 | 0.0390 | 0.4354 | 0.781 | Oscillations died out | 6000 s | n/a | Max of 20% at 5 | At 3 | MEA5-25-constco-flooding-cathodeup |
| h-ii | co | 12 | 6 | 0.1270 | 0.1718 | 0.1814 | 0.1827 | 0.1358 | 0.1005 | 0.5109 | 0.899 | Redistribution after 2000 s | 2500 s | n/a | n/a | At 4 | MEA5-25-constco-flooding-cathodeup |
| h-ii | co | 6 | 3 | 0.0833 | 0.1116 | 0.1203 | 0.1172 | 0.1186 | 0.1307 | 0.3826 | 0.562 | Start up to stable operation | 12,000 s | n/a | n/a | n/a | MEA5-25-constco-flooding-cathodeup2 |
| h-ii | co | 12 | 6 | 0.1110 | 0.1488 | 0.1516 | 0.1223 | 0.0717 | 0.0379 | 0.3600 | 0.643 | Oscillations | 75,000 s | 2600 s | 25% at 4, 5, & 6 | At 3 | MEA5-25-constco-flooding-cathodeup3 |

**Appendix. (Continued)**

| Flow Configuration | Flow Direction | QH2 | QO2 | i1 | i2 | i3 | i4 | i5 | i6 | V | itot | Stability | Duration | Period of oscillations | Max. (by seg.) magnitude of fluctuations | Phase change | File name |
|---|---|---|---|---|---|---|---|---|---|---|---|---|---|---|---|---|---|
| h-ii | co | 6 | 3 | 0.1076 | 0.1450 | 0.1451 | 0.1036 | 0.0540 | 0.0283 | 0.3220 | 0.584 | Irregular spiked fluctuations | 15,000 s | 2500 s | 10% at 4, 5, & 6, none at 1–3 | n/a | MEA5-25-constco-flooding-cathodeup3 |
| h-ii | co | 4 | 2 | 0.1041 | 0.1370 | 0.1280 | 0.0783 | 0.0388 | 0.0207 | 0.2760 | 0.507 | Irregular spiked fluctuations | 5500 s | n/a | n/a | n/a | MEA5-25-constco-flooding-cathodeup3 |
| h-iii | cnt | 12 | 6 | 0.0814 | 0.1131 | 0.1508 | 0.1778 | 0.1724 | 0.1719 | 0.4957 | 0.867 | Steady | 60,000 s | n/a | n/a | n/a | MEA5-25-constcnt-flooding-horizontal |
| h-iii | cnt | 12 | 6 | 0.1150 | 0.1303 | 0.1335 | 0.1395 | 0.1536 | 0.1659 | 0.4814 | 0.838 | Steady | 60,000 s | n/a | n/a | n/a | MEA5-25-constcnt-flooding-horizontal2 |
| h-iii | cnt | 6 | 3 | 0.1265 | 0.1425 | 0.1447 | 0.1390 | 0.1285 | 0.1084 | 0.4531 | 0.789 | Irregular spiked fluctuations | 23,000 s | ~2800 s for large spikes | Max of 50% at 6 | Between 3 & 4 | MEA5-25-constcnt-flooding-horizontal2-cont |
| h-iii | cnt | 12 | 3 | 0.1256 | 0.1420 | 0.1441 | 0.1387 | 0.1290 | 0.1092 | 0.4523 | 0.789 | Irregular spiked fluctuations | 4200 s | ~1200 s for large spikes | Max of 45% at 6 | Between 3 & 4 | MEA5-25-constcnt-flooding-horizontal2-cont |
| h-iii | cnt | 12 | 6 | 0.1089 | 0.1249 | 0.1314 | 0.1405 | 0.1589 | 0.1792 | 0.4874 | 0.844 | Steady | 4200 s | n/a | n/a | n/a | MEA5-25-constcnt-flooding-horizontal2-cont |
| h-iii | cnt | 6 | 3 | 0.0977 | 0.1370 | 0.1738 | 0.1722 | 0.1246 | 0.0960 | 0.4522 | 0.801 | Irregular spiked fluctuations | 10,500 s | 2200 s | Max of 60% at 6 | Between 3 & 4 | MEA5-25-constcnt-flooding-horizontal-cont |
| h-iii | cnt | 7 | 3.5 | 0.0779 | 0.1121 | 0.1530 | 0.1873 | 0.1795 | 0.1768 | 0.5056 | 0.887 | Steady | 3000 s | n/a | n/a | n/a | MEA5-25-constcnt-flooding-horizontal-cont |
| h-iii | cnt | 10 | 10 | 0.0305 | 0.0435 | 0.0585 | 0.0713 | 0.0701 | 0.0689 | 0.6995 | 0.343 | Steady | 5700 s | n/a | n/a | n/a | MEA5-25-constcnt-flooding-horizontal-cont2 |
| h-iii | cnt | 6 | 3 | 0.0309 | 0.0438 | 0.0591 | 0.0710 | 0.0692 | 0.0680 | 0.6955 | 0.342 | Steady | 64,000 s | n/a | n/a | n/a | MEA5-25-constcnt-flooding-horizontal-cont2 |
| h-iii | co | 6 | 3 | 0.1556 | 0.2158 | 0.1820 | 0.1177 | 0.0570 | 0.0310 | 0.4263 | 0.759 | Stable - small oscillations | 14,000 s | 75 s | 3% at 4 | Between 2 & 3 | MEA5-25-constco-droplets2 |
| h-iii | co | 12 | 6 | 0.1020 | 0.1540 | 0.1660 | 0.1723 | 0.1577 | 0.1543 | 0.5180 | 0.906 | Steady | 5000 s | n/a | n/a | n/a | MEA5-25-constco-droplets2 |
| h-iii | co | 6 | 3 | 0.0830 | 0.1270 | 0.1084 | 0.1092 | 0.1140 | 0.1290 | 0.3777 | 0.671 | Steady | 60,000 s | n/a | n/a | n/a | MEA5-25-constco-flooding-horizontal |
| h-iii | co | 12 | 6 | 0.0940 | 0.1376 | 0.1141 | 0.1133 | 0.1210 | 0.1425 | 0.4080 | 0.722 | Steady | 100.000 s | n/a | n/a | n/a | MEA5-25-constco-flooding-horizontal |
| h-iii | co | 6 | 3 | 0.0951 | 0.1392 | 0.1154 | 0.1138 | 0.1213 | 0.1435 | 0.4096 | 0.728 | Minor fluctuations | 5000 s | n/a | n/a | n/a | MEA5-25-constco-flooding-horizontal |
| h-iii | co | 5 | 2.5 | 0.1015 | 0.1495 | 0.1198 | 0.1066 | 0.0894 | 0.0661 | 0.3521 | 0.633 | Irregular fluctuations | 10,000 s | 2000 s | Max of 30% at 6 | Between 2 & 3 | MEA5-25-constco-flooding-horizontal |
| h-iii | co | 6 | 3 | 0.1112 | 0.1594 | 0.1267 | 0.1177 | 0.1184 | 0.1336 | 0.4337 | 0.768 | Oscillations with spikes | 250,000 s | 2000 s | 10% at 6 | At 4 | MEA5-25-constco-flooding-horizontal |
| v-i | cnt | 10 | 10 | 0.0756 | 0.1123 | 0.1481 | 0.1825 | 0.1606 | 0.1645 | 0.4726 | 0.844 | Steady | 10,000 s | n/a | n/a | n/a | MEA5-25-constcnt-flooding-h2inletdown |
| v-i | cnt | 6 | 3 | 0.0915 | 0.1327 | 0.1648 | 0.1680 | 0.1152 | 0.0950 | 0.4281 | 0.767 | Irregular spiked fluctuations | 5000 s | 1700 s | Max of 40% at 6 | Between 3 & 4 | MEA5-25-constcnt-flooding-h2inletdown |

**Appendix. (Continued)**

| Flow Configuration | Flow Direction | QH2 | QO2 | i1 | i2 | i3 | i4 | i5 | i6 | V | itot | Stability | Duration | Period of oscillations | Max. (by seg.) magnitude of fluctuations | Phase change | File name |
|---|---|---|---|---|---|---|---|---|---|---|---|---|---|---|---|---|---|
| v-i | co | 12 | 6 | 0.0859 | 0.1200 | 0.1295 | 0.1474 | 0.1326 | 0.1064 | 0.4074 | 0.722 | Steady | 67,000 s | n/a | n/a | n/a | MEA5-25-constco-flooding-inletsup |
| v-i | co | 6 | 3 | 0.0851 | 0.1190 | 0.1299 | 0.1479 | 0.1331 | 0.1066 | 0.4058 | 0.722 | Small fluctuations | 7000 s | n/a | n/a | n/a | MEA5-25-constco-flooding-inletsup |
| v-i | co | 8 | 2.7 | 0.0873 | 0.1214 | 0.1299 | 0.1426 | 0.1208 | 0.0927 | 0.3880 | 0.695 | Spiked oscillations | 2000 s | 3200 s | Max of 20% at 6 | Between 3 and 4 | MEA5-25-constco-flooding-inletsup |
| v-ii | cnt | 10 | 10 | 0.0731 | 0.1115 | 0.1484 | 0.1857 | 0.1731 | 0.1745 | 0.4879 | 0.866 | Steady | 72,000 s | n/a | n/a | n/a | MEA5-25-constcnt-flooding-o2inletdown |
| v-ii | cnt | 6 | 3 | 0.0540 | 0.0977 | 0.1526 | 0.1973 | 0.1565 | 0.1451 | 0.4482 | 0.803 | Oscillations | 18,000 s | 25–40 s | 20% at 6 | At 4 | MEA5-25-constcnt-flooding-o2inletdown |
| v-ii | cnt | 10 | 10 | 0.0766 | 0.1036 | 0.1425 | 0.1923 | 0.1774 | 0.2010 | 0.5032 | 0.894 | Steady | 3500 s | n/a | n/a | | MEA5-25-constcnt-flooding-o2inletdown |
| v-ii | cnt | 8 | 4 | 0.0712 | 0.1003 | 0.1435 | 0.1948 | 0.1785 | 0.2009 | 0.4996 | 0.889 | Steady | 4300 s | n/a | n/a | n/a | MEA5-25-constcnt-flooding-o2inletdown |
| v-ii | cnt | 12 | 6 | 0.0790 | 0.1069 | 0.1517 | 0.1625 | 0.1640 | 0.1729 | 0.4764 | 0.837 | Steady | 78,000 s | n/a | n/a | n/a | MEA5-25-constcnt-flooding-o2inletdown2 |
| v-ii | cnt | 6 | 3 | 0.0912 | 0.1221 | 0.1692 | 0.1632 | 0.1362 | 0.1033 | 0.4434 | 0.785 | Irregular fluctuations | 14,000 s | n/a | Max of 40% at 6 | Between 3 & 4 | MEA5-25-constcnt-flooding-o2inletdown2 |
| v-ii | cnt | 12 | 3 | 0.0956 | 0.1274 | 0.1741 | 0.1624 | 0.1243 | 0.0830 | 0.4318 | 0.767 | Irregular fluctuations | 4000 s | n/a | Max of 35% at 6 | Between 3 & 4 | MEA5-25-constcnt-flooding-o2inletdown2 |
| v-ii | cnt | 5 | 2.5 | 0.1169 | 0.1482 | 0.1784 | 0.1127 | 0.0512 | 0.0278 | 0.3516 | 0.635 | Irregular fluctuations | 4000 s | n/a | Max of 10% at 4 | Between 2 & 3 | MEA5-25-constcnt-flooding-o2inletdown2 |
| v-ii | cnt | 10 | 10 | 0.0787 | 0.1053 | 0.1547 | 0.1713 | 0.1744 | 0.1780 | 0.4930 | 0.862 | Steady | 149,000 s | n/a | n/a | n/a | MEA5-25-constcnt-flooding-o2inletdown2-cont |
| v-ii | cnt | 12 | 3.5 | 0.0803 | 0.1077 | 0.1584 | 0.1731 | 0.1706 | 0.1676 | 0.4880 | 0.858 | Irregular spiked fluctuations | 20,000 s | 1600 s | Max of 20% at 6 | Between 4 & 5 | MEA5-25-constcnt-flooding-o2inletdown2-cont |
| v-ii | cnt | 6 | 3 | 0.1013 | 0.1347 | 0.1873 | 0.1682 | 0.1131 | 0.0635 | 0.4319 | 0.768 | Irregular fluctuations | 8000 s | n/a | Max of 50% at 5 | Between 3 & 4 | MEA5-25-constcnt-flooding-o2inletdown2-cont |
| v-ii | co | 12 | 6 | 0.1165 | 0.1606 | 0.1731 | 0.1701 | 0.1435 | 0.1466 | 0.5204 | 0.911 | Steady | 56,000 s | n/a | n/a | n/a | MEA5-25-constco-droplets1 |
| v-ii | co | 6 | 3 | 0.1928 | 0.2424 | 0.2003 | 0.0863 | 0.0294 | 0.0166 | 0.4325 | 0.768 | Minor fluctuations | 17,000 s | n/a | n/a | n/a | MEA5-25-constco-droplets1 |
| v-ii | co | 12 | 3 | 0.0083 | 0.0101 | 0.0114 | 0.0139 | 0.0165 | 0.0239 | 0.0281 | 0.085 | Regular oscillations | 7000 s | 60 s then 15 s | 65% at 6 then 60% at 4 | Between 3 & 4, then at 3 | MEA5-25-constco-droplets1 |
| v-ii | co | 12 | 6 | 0.0091 | 0.0152 | 0.0335 | 0.0714 | 0.0843 | 0.1038 | 0.1626 | 0.317 | Stable for ~ 100 s then oscillations | 3000 s | 43 s | Oscillations of 200–300% | | MEA5-25-constco-droplets1 |
| v-ii | co | 7 | 3.5 | 0.1232 | 0.1652 | 0.1669 | 0.1704 | 0.1294 | 0.1260 | 0.5008 | 0.881 | Irregular fluctuations | 81,000 s | n/a | Max of 20% at 6 | Between 4 & 5 | MEA5-25-constco-flooding-inletsdown |
| v-ii | co | 6 | 3 | 0.1596 | 0.1987 | 0.1748 | 0.1455 | 0.0713 | 0.0453 | 0.4466 | 0.795 | Irregular fluctuations | 5000 s | n/a | Max of 40% at 4 | Between 2 & 3 | MEA5-25-constco-flooding-inletsdown |
| v-ii | co | 12 | 3 | 0.1649 | 0.2040 | 0.1785 | 0.1378 | 0.0622 | 0.0394 | 0.4403 | 0.787 | Minor fluctuations | 1500 s | n/a | n/a | n/a | MEA5-25-constco-flooding-inletsdown |
| v-ii | co | 12 | 4 | 0.1213 | 0.1614 | 0.1665 | 0.1770 | 0.1406 | 0.1405 | 0.5147 | 0.904 | Large oscillations at segment 6 | 3000 s | 400 s | 50% at 6 | Between 4 & 5 | MEA5-25-constco-flooding-inletsdown |
| v-ii | co | 7 | 3.5 | 0.1684 | 0.2113 | 0.1824 | 0.1364 | 0.0538 | 0.0347 | 0.4419 | 0.787 | Small oscillations | 12,000 s | 8 s | 45% at 5 | Between 3 & 4 | MEA5-25-constco-flooding-inletsdown |

**Appendix. (Continued)**

| Flow Configuration | Flow Direction | QH2 | QO2 | i1 | i2 | i3 | i4 | i5 | i6 | V | itot | Stability | Duration | Period of oscillations | Max. (by seg.) magnitude of fluctuations | Phase change | File name |
|---|---|---|---|---|---|---|---|---|---|---|---|---|---|---|---|---|---|
| v-ii | co | 10 | 5 | 0.1384 | 0.1637 | 0.1413 | 0.1615 | 0.1457 | 0.1955 | 0.5430 | 0.946 | Steady | 6000 s | n/a | n/a | n/a | MEA5-25-constco-flooding-inletsdown2 |
| v-ii | co | 7 | 3.5 | 0.1757 | 0.2026 | 0.1626 | 0.1582 | 0.1001 | 0.0858 | 0.5043 | 0.885 | Steady after a few fluctuations | 5000 s | n/a | n/a | n/a | MEA5-25-constco-flooding-inletsdown2 |
| v-ii | co | 6 | 3 | 0.2391 | 0.2440 | 0.1433 | 0.0874 | 0.0347 | 0.0214 | 0.4306 | 0.77 | Minor fluctuations | 5000 s | n/a | n/a | n/a | MEA5-25-constco-flooding-inletsdown2 |
| v-ii | co | 8 | 4 | 0.1451 | 0.1742 | 0.1512 | 0.1723 | 0.1477 | 0.1517 | 0.5410 | 0.942 | Oscillations with varying phase | 80,000 s | 300 s | Max of 30% at 6 | Between 4 & 5 | MEA5-25-constco-flooding-inletsdown2 |
| v-ii | co | 8 | 4 | 0.0053 | 0.0058 | 0.0064 | 0.0071 | 0.0088 | 0.0132 | 0.0044 | 0.0466 | Oscillations going from zero to high | 14,000 s | 550 s | 0–25 A at 6 | All in phase | MEA5-25-constco-flooding-inletsdown2 |
| v-ii | co | 8 | 4 | 0.0051 | 0.0061 | 0.0075 | 0.0112 | 0.0157 | 0.0274 | 0.0215 | 0.073 | Oscillations died out then irregular fluctuations | 37,000 s | n/a | n/a | n/a | MEA5-25-constco-flooding-inletsdown2 |

**Description of columns**
**Configuration:** Designates one of three horizontal or two vertical configurations.
**Flow direction:** Designates either co-current or counter-current flow pattern.
**QH2, QO2:** Flow rates in mL/min of hydrogen and oxygen, respectively.
**i1–i6:** Local currents in A from each of the anode segments 1–6 defined with the oxygen inlet closest to segment 1.
***V*:** Voltage in V measured across the external load in the fuel cell circuit.
**itot:** Total current in A produced by the fuel cell.
**Stability:** Describes the type and degree of any fluctuations in the local current.
**Duration:** Gives how long the particular state of the fuel cell's performance persisted.
**Period of oscillations:** Gives the approximate period of the oscillations or fluctuations.
**Max. (by. seg) magnitude of fluctuations:** Gives the magnitude of the fluctuations based on the local current from the segment exhibiting the largest fluctuations.
**Phase change:** Describes the point along the flow channel at which the local current response to changes in flow or to liquid water slugs switches between increasing and decreasing.
**File name:** Gives the name of the raw data file.